

Journal of
Mechanics of
Materials and Structures

**AN ENERGY-MOMENTUM CONSERVING ALGORITHM FOR
NONLINEAR TRANSIENT ANALYSIS WITHIN THE FRAMEWORK
OF HYBRID ELEMENTS**

C. S. Jog and Phani Motamarri

Volume 4, N^o 1

January 2009



mathematical sciences publishers

AN ENERGY-MOMENTUM CONSERVING ALGORITHM FOR NONLINEAR TRANSIENT ANALYSIS WITHIN THE FRAMEWORK OF HYBRID ELEMENTS

C. S. JOG AND PHANI MOTAMARRI

This work deals with the formulation and implementation of an energy-momentum conserving algorithm for conducting the nonlinear transient analysis of structures, within the framework of stress-based hybrid elements. Hybrid elements, which are based on a two-field variational formulation, are much less susceptible to locking than conventional displacement-based elements within the static framework. We show that this advantage carries over to the transient case, so that not only are the solutions obtained more accurate, but they are obtained in fewer iterations. We demonstrate the efficacy of the algorithm on a wide range of problems such as ones involving dynamic buckling, complicated three-dimensional motions, et cetera.

1. Introduction

In the absence of loading in a pure traction initial boundary-value problem, the linear and angular momenta, and, if the body is elastic, the energy as well, are conserved. [Simo and Tarnow \[1992; 1994\]](#) were the first to develop algorithmic approximations that would, similarly to continuum dynamics, conserve these properties. Since with the use of these schemes there is no blow-up of the solution in the absence of loading, these algorithms can be said to be inherently stable. For this reason, there has been an extensive literature on these classes of time stepping algorithms. [Laursen and Meng \[2001\]](#) and [Gonzalez \[2000\]](#) extended the method of Simo and Tarnow to nonlinear constitutive models, albeit by different methods. [Brank et al. \[1998\]](#) and [Sansour et al. \[2004\]](#) considered the application of these methods to the motion of shells. [Betsch and Steinmann \[2001\]](#) developed a time finite element method and introduced the assumed strain method in time which simplifies the design of energy-momentum conserving algorithms for nonlinear constitutive models. [Armero and Romero \[2001a; 2001b\]](#), [Bauchau and Joo \[1999; 2003\]](#), and [Kuhl et al. \[Kuhl and Crisfield 1999; Kuhl and Ramm 1996; 1999\]](#) introduced the use of unconditionally stable energy-momentum conserving time-integration schemes with high-frequency numerical dissipation. [Balah and Al-Ghamedy \[2005\]](#) extended the method of Simo and Tarnow to the nonlinear dynamics of laminated shells. Most of the works cited above including that of Simo and Tarnow use the displacement-based formulation.

It is well known that the standard displacement-based formulation locks in the case of static problems for shell-type structures, and the adverse effects of this over stiff stiffness matrix are also seen in transient problems. Ever since the pioneering work of [Pian et al. \[Pian and Sumihara 1984; Pian and Tong 1986\]](#), it has been known that hybrid stress-based formulations are much less susceptible to locking than the standard displacement-based formulation. Our goal in this work, which is a generalization of the work

Keywords: nonlinear transient analysis, hybrid elements, energy-momentum conservation.
We gratefully acknowledge the financial support of the ISRO-IISc Space Technology Cell.

in [Jog and Kelkar 2006] to transient problems, is to develop the formulation and implementation of an energy-momentum conserving time stepping strategy for three-dimensional hexahedral and axisymmetric hybrid stress elements.

As pointed out in [Jog and Kelkar 2006], since the treatment is fully three-dimensional, it can be used (with no modification of the formulation) in tackling problems as diverse as shells with variable thickness, laminated composites, ply drop-offs on the one hand, and problems with thick geometries on the other. Material nonlinearities are also handled easily since no reduction of the three-dimensional constitutive relations based on plane-stress assumptions or any other such assumption needs to be carried out.

In Section 2, we present a two-field variational formulation for the transient nonlinear elasticity problem that enforces the balance of the linear momentum and the traction boundary condition, and the strain-displacement relations in a weak sense. These variational statements are then linearized and discretized in Section 3 to develop an incremental total Lagrangian finite element formulation. Next we show that the stress interpolation function for higher-order hybrid elements, which are derived based on static considerations alone, have to be modified slightly in order to prevent instabilities that can arise during transient solutions of some problems. Several challenging numerical examples which include problems involving dynamic buckling, impact problems, complicated three-dimensional motions of shell-type structures, et cetera are presented in Section 4. We shall see in this section that not only do we obtain good coarse-mesh accuracy, but also obtain the solutions to many demanding problems with comparatively large time steps. Section 5 presents the conclusions.

We note the conventions followed throughout this work. Scalars are denoted by lightface letters, while vectors and higher-order tensors are denoted by boldface letters. $\mathbf{A} \cdot$ denotes contraction over one index, and a colon contraction over two indices. For example, $\mathbf{t} \cdot \mathbf{u} = t_i u_i$, $\mathbf{S} : \mathbf{E} = S_{ij} E_{ij}$, et cetera, with the summation convention over repeated indices implied. If $\mathbf{G}(\mathbf{T})$ is a tensor-valued function of a tensor \mathbf{T} , the directional derivative of \mathbf{G} evaluated at \mathbf{T} in the direction \mathbf{U} , defined by

$$D\mathbf{G}(\mathbf{T})[\mathbf{U}] := \left. \frac{d}{d\alpha} \mathbf{G}(\mathbf{T} + \alpha\mathbf{U}) \right|_{\alpha=0}, \quad (1)$$

will play a key role in the linearizations that are carried out during the finite element formulation.

2. Formulation

In this section, we first present the two-field variational formulation that is later used to derive the finite element equations. Since the deformed configuration is not known in advance, all equations are written with respect to the reference configuration Ω whose boundary Γ is composed of two open, disjoint regions: $\Gamma = \bar{\Gamma}_u \cup \bar{\Gamma}_t$. The spatial variables in the reference and deformed configurations are denoted by \mathbf{X} and \mathbf{x} , respectively. We assume a one-to-one mapping χ that takes \mathbf{X} to \mathbf{x} , that is, $\mathbf{x} = \chi(\mathbf{X}, t) = \mathbf{X} + \mathbf{u}(\mathbf{X}, t)$, where \mathbf{u} is the displacement field. The deformation gradient is given by $\mathbf{F} := \nabla \chi = \mathbf{I} + \nabla \mathbf{u}$, where the gradient is with respect to the material coordinates \mathbf{X} ; the traction \mathbf{t}^0 is given by $\mathbf{F} \mathbf{S} \mathbf{n}^0$; and we let

$$\bar{\mathbf{E}}(\mathbf{u}) := \frac{1}{2} [(\nabla \mathbf{u}) + (\nabla \mathbf{u})^T + (\nabla \mathbf{u})^T (\nabla \mathbf{u})]. \quad (2)$$

Within the context of the two-field variational formulation developed below, the strains are recovered from the stresses by means of the constitutive relation

$$\mathbf{E} = \hat{\mathbf{E}}(\mathbf{S}) \text{ on } \Omega. \quad (3)$$

This does not imply that the stress-strain relation $\mathbf{S} = \hat{\mathbf{S}}(\mathbf{E})$ has to be analytically inverted—only that, given the state of stress, we find the state of strain using the stress-strain relation as discussed in [Jog and Kelkar 2006].

The two-field variational principle on which our finite element formulation is based enforces the balance of linear momentum, traction boundary condition, and the strain-displacement relation in a weak sense. If

$$V_u := \{\mathbf{u}_\delta \in H^1(\Omega) : \mathbf{u}_\delta = \mathbf{0} \text{ on } \Gamma_u\}, \quad V_S := \{\mathbf{S}_\delta \in L^2(\Omega) : \mathbf{S}_\delta^T = \mathbf{S}_\delta \text{ on } \Omega\},$$

denote the space of variations of the displacements and the second Piola–Kirchhoff stress, the two-field variational formulation obtained after incorporating the transient terms in the formulation presented in [Jog and Kelkar 2006] is given by

$$\int_\Omega \rho_0 \mathbf{u}_\delta \cdot \frac{\partial \mathbf{v}}{\partial t} d\Omega + \int_\Omega \mathbf{S} : \bar{\mathbf{E}}_\delta d\Omega = \int_\Omega \rho_0 \mathbf{u}_\delta \cdot \mathbf{b}^0 d\Omega + \int_{\Gamma_t} \mathbf{u}_\delta \cdot \bar{\mathbf{t}}^0 d\Gamma, \quad \forall \mathbf{u}_\delta \in V_u, \quad (4)$$

$$\int_\Omega \mathbf{S}_\delta : [\bar{\mathbf{E}}(\mathbf{u}) - \hat{\mathbf{E}}(\mathbf{S})] d\Omega = 0, \quad \forall \mathbf{S}_\delta \in V_S, \quad (5)$$

where $\bar{\mathbf{E}}$ is given by (2), and its variation $\bar{\mathbf{E}}_\delta$ is given by

$$\bar{\mathbf{E}}_\delta(\mathbf{u}, \mathbf{u}_\delta) = \frac{1}{2} [\mathbf{F}^T \nabla \mathbf{u}_\delta + (\nabla \mathbf{u}_\delta)^T \mathbf{F}] = \frac{1}{2} [(\nabla \mathbf{u}_\delta) + (\nabla \mathbf{u}_\delta)^T + (\nabla \mathbf{u})^T (\nabla \mathbf{u}_\delta) + (\nabla \mathbf{u}_\delta)^T (\nabla \mathbf{u})]. \quad (6)$$

In this variational formulation, $\rho_0 = (\det \mathbf{F})\rho$ is the density in the reference configuration in terms of the density ρ in the deformed configuration, \mathbf{v} is the velocity, \mathbf{n}^0 is the outward normal to Γ , $\mathbf{t}^0 := \|(\text{cof } \mathbf{F})\mathbf{n}^0\| \mathbf{t}$ are the tractions defined on the reference configuration in terms of the actual tractions \mathbf{t} on the deformed configuration, and $\mathbf{b}^0(\mathbf{X}, t) := \mathbf{b}(\boldsymbol{\chi}(\mathbf{X}, t))$ is the body force field on the reference configuration.

In what follows, we shall develop a time stepping strategy where we focus attention on a typical time interval $[t_n, t_{n+1}]$, and let $t_\Delta := t_{n+1} - t_n$ denote the corresponding time step size. The variables at times t_n and t_{n+1} will be denoted by the subscripts n and $n+1$, respectively. We consider the material to be hyperelastic with strain-energy density function $\hat{W}(\mathbf{E})$, so that the stress is given by

$$\mathbf{S} = \frac{\partial \hat{W}}{\partial \mathbf{E}}.$$

Within the context of our two-field variational formulation, we propose the following time stepping scheme which, as we shall subsequently show, conserves linear and angular momentum and energy in the absence of loading:

$$\frac{\mathbf{x}_{n+1} - \mathbf{x}_n}{t_\Delta} = \frac{\mathbf{u}_{n+1} - \mathbf{u}_n}{t_\Delta} = \frac{\mathbf{v}_n + \mathbf{v}_{n+1}}{2}, \quad (7)$$

$$\begin{aligned} \int_\Omega \rho_0 \mathbf{u}_\delta \cdot \left(\frac{\mathbf{v}_{n+1} - \mathbf{v}_n}{t_\Delta} \right) d\Omega + \int_\Omega \left(\frac{\bar{\mathbf{E}}_\delta)_n + (\bar{\mathbf{E}}_\delta)_{n+1}}{2} \right) : \mathbf{S}_{\text{alg}} d\Omega \\ = \int_\Omega \rho_0 \mathbf{u}_\delta \cdot \mathbf{b}_{\text{alg}} d\Omega + \int_{\Gamma_t} \mathbf{u}_\delta \cdot \bar{\mathbf{t}}_{\text{alg}} d\Gamma, \quad \forall \mathbf{u}_\delta \in V_u, \end{aligned} \quad (8)$$

$$\int_{\Omega} \mathbf{S}_{\delta} : [\bar{\mathbf{E}}(\mathbf{u}_m) - \hat{\mathbf{E}}(\mathbf{S}_m)] d\Omega = 0, \quad m = n, n+1, \quad \forall \mathbf{S}_{\delta} \in V_S, \quad (9)$$

where $\mathbf{b}_{\text{alg}} = (\mathbf{b}_n^0 + \mathbf{b}_{n+1}^0)/2$, $\bar{\mathbf{t}}_{\text{alg}} = (\bar{\mathbf{t}}_n^0 + \bar{\mathbf{t}}_{n+1}^0)/2$, and, in terms of $\tilde{\mathbf{E}}(\zeta) := [(1-\zeta)\mathbf{E}_n + (1+\zeta)\mathbf{E}_{n+1}]/2$, the algorithmic stress \mathbf{S}_{alg} given by

$$\mathbf{S}_{\text{alg}} = \frac{1}{2} \int_{-1}^1 \frac{\partial W(\tilde{\mathbf{E}})}{\partial \tilde{\mathbf{E}}} d\zeta, \quad (10)$$

This formula is similar to that presented in [Betsch and Steinmann 2001], except that here \mathbf{E} denotes the strain recovered from the constitutive relation, and not from the strain-displacement relation.

We now prove that as in the continuum problem, for the pure traction initial boundary-value problem, in the absence of tractions and body forces ($\bar{\mathbf{t}}_{\text{alg}} = \mathbf{b}_{\text{alg}} = \mathbf{0}$), the linear and angular momenta, and total (kinetic plus strain) energy are conserved.

2.1. Discrete linear and angular momentum conservation. To prove that the discrete linear momentum is conserved, choose for all time $\mathbf{u}_{\delta} = \mathbf{c}$ in (8), where \mathbf{c} is a constant vector. This choice is permissible since the entire boundary is free of displacement constraints. With this choice $(\bar{\mathbf{E}}_{\delta})_n = (\bar{\mathbf{E}}_{\delta})_{n+1} = \mathbf{0}$, and we get

$$\mathbf{c} \cdot \int_{\Omega} \rho_0 (\mathbf{v}_{n+1} - \mathbf{v}_n) d\Omega = 0,$$

which by virtue of the arbitrariness of \mathbf{c} , proves the conservation of the discrete linear momentum.

To prove the conservation of the discrete angular momentum, $\mathbf{J}_{n+1} = \mathbf{J}_n$, choose

$$\mathbf{u}_{\delta} = \mathbf{c} \times (\mathbf{x}_n + \mathbf{x}_{n+1}) = \mathbf{W}(\mathbf{x}_n + \mathbf{x}_{n+1}),$$

where \mathbf{W} is the skew-symmetric tensor of which \mathbf{c} is the axial vector. Substituting $\nabla \mathbf{u}_{\delta} = \mathbf{W}(\mathbf{F}_n + \mathbf{F}_{n+1})$ into (6), we get

$$(\bar{\mathbf{E}}_{\delta})_n + (\bar{\mathbf{E}}_{\delta})_{n+1} = \frac{1}{2} [(\mathbf{F}_n + \mathbf{F}_{n+1})^T \mathbf{W}(\mathbf{F}_n + \mathbf{F}_{n+1}) + (\mathbf{F}_n + \mathbf{F}_{n+1})^T \mathbf{W}^T(\mathbf{F}_n + \mathbf{F}_{n+1})] = \mathbf{0}.$$

Using the property $(\mathbf{p} \times \mathbf{q}) \cdot \mathbf{r} = \mathbf{p} \cdot (\mathbf{q} \times \mathbf{r})$, the first term in (8) simplifies to

$$\begin{aligned} & \int_{\Omega} \rho_0 \mathbf{c} \cdot (\mathbf{x}_n + \mathbf{x}_{n+1}) \times \left(\frac{\mathbf{v}_{n+1} - \mathbf{v}_n}{t_{\Delta}} \right) d\Omega \\ &= \frac{1}{t_{\Delta}} \mathbf{c} \cdot \int_{\Omega} \rho_0 [2(\mathbf{x}_{n+1} \times \mathbf{v}_{n+1} - \mathbf{x}_n \times \mathbf{v}_n) - (\mathbf{x}_{n+1} - \mathbf{x}_n) \times (\mathbf{v}_n + \mathbf{v}_{n+1})] d\Omega = \frac{2}{t_{\Delta}} \mathbf{c} \cdot [\mathbf{J}_{n+1} - \mathbf{J}_n], \end{aligned}$$

the last equality following by (7). Thus, with the given choice of \mathbf{u}_{δ} and in the absence of loading, (8) reduces to

$$\mathbf{c} \cdot [\mathbf{J}_{n+1} - \mathbf{J}_n] = 0,$$

which by virtue of the arbitrariness of \mathbf{c} leads to $\mathbf{J}_{n+1} = \mathbf{J}_n$.

By multiplying the spatially discretized versions of (8) and (9) by the vectors

$$[c_1 \ c_2 \ c_3 \ c_1 \ c_2 \ c_3 \ \dots]_{1 \times N} \quad \text{and} \quad [-c_3 z_2^{(1)} + c_2 z_3^{(1)} \quad c_3 z_1^{(1)} - c_1 z_3^{(1)} \quad -c_2 z_1^{(1)} + c_1 z_2^{(1)} \quad \dots]_{1 \times N},$$

where N is the total number of displacement degrees of freedom, c_1 , c_2 , and c_3 are constants, and $\mathbf{z}^{(i)} = \mathbf{x}_n^{(i)} + \mathbf{x}_{n+1}^{(i)}$, where i denotes the node number, we can show that the linear and angular momenta are conserved even after spatial discretization has been carried out.

2.2. Discrete energy conservation. To prove conservation of energy for a hyperelastic material with \mathbf{S}_{alg} given by (10), we choose $\mathbf{u}_\delta = \mathbf{u}_{n+1} - \mathbf{u}_n = \mathbf{x}_{n+1} - \mathbf{x}_n$. Substituting $\nabla \mathbf{u}_\delta = \mathbf{F}_{n+1} - \mathbf{F}_n$ into (6), we get

$$(\bar{\mathbf{E}}_\delta)_n + (\bar{\mathbf{E}}_\delta)_{n+1} = [\mathbf{F}_{n+1}^T \mathbf{F}_{n+1} - \mathbf{F}_n^T \mathbf{F}_n] = 2[\bar{\mathbf{E}}_{n+1} - \bar{\mathbf{E}}_n]. \quad (11)$$

On choosing $\mathbf{S}_\delta = \mathbf{S}_{\text{alg}}$ in (9) (this choice is permissible since $\mathbf{S}_{\text{alg}} \in V_S$), we have

$$\int_{\Omega} [\bar{\mathbf{E}}(\mathbf{u}_n) - \hat{\mathbf{E}}(\mathbf{S}_n)] : \mathbf{S}_{\text{alg}} d\Omega = 0, \quad \int_{\Omega} [\bar{\mathbf{E}}(\mathbf{u}_{n+1}) - \hat{\mathbf{E}}(\mathbf{S}_{n+1})] : \mathbf{S}_{\text{alg}} d\Omega = 0,$$

which leads to

$$\int_{\Omega} [\bar{\mathbf{E}}(\mathbf{u}_{n+1}) - \bar{\mathbf{E}}(\mathbf{u}_n)] : \mathbf{S}_{\text{alg}} d\Omega = \int_{\Omega} [\hat{\mathbf{E}}(\mathbf{S}_{n+1}) - \hat{\mathbf{E}}(\mathbf{S}_n)] : \mathbf{S}_{\text{alg}} d\Omega. \quad (12)$$

Using (11) and (12), the second term in (8) simplifies to

$$\begin{aligned} \int_{\Omega} \left[\frac{(\bar{\mathbf{E}}_\delta)_n + (\bar{\mathbf{E}}_\delta)_{n+1}}{2} \right] : \mathbf{S}_{\text{alg}} d\Omega &= \int_{\Omega} [\hat{\mathbf{E}}(\mathbf{S}_{n+1}) - \hat{\mathbf{E}}(\mathbf{S}_n)] : \mathbf{S}_{\text{alg}} \\ &= \int_{\Omega} \frac{\partial \tilde{\mathbf{E}}}{\partial \tilde{\boldsymbol{\zeta}}} : \int_{-1}^1 \frac{\partial W(\tilde{\mathbf{E}})}{\partial \tilde{\mathbf{E}}} d\tilde{\boldsymbol{\zeta}} \quad (\text{by (10)}) \\ &= \int_{\Omega} \int_{-1}^1 \frac{\partial W(\tilde{\mathbf{E}}(\tilde{\boldsymbol{\zeta}}))}{\partial \tilde{\boldsymbol{\zeta}}} d\tilde{\boldsymbol{\zeta}} = [\hat{W}_{n+1} - \hat{W}_n]. \end{aligned}$$

On using (7), the first term in (8) simplifies to

$$\begin{aligned} \int_{\Omega} \rho_0(\mathbf{u}_{n+1} - \mathbf{u}_n) \left(\frac{\mathbf{v}_{n+1} - \mathbf{v}_n}{t_\Delta} \right) d\Omega &= \frac{1}{2} \int_{\Omega} \rho_0(\mathbf{v}_{n+1} + \mathbf{v}_n) \cdot (\mathbf{v}_{n+1} - \mathbf{v}_n) d\Omega \\ &= \frac{1}{2} \int_{\Omega} \rho_0(\mathbf{v}_{n+1} \cdot \mathbf{v}_{n+1} - \mathbf{v}_n \cdot \mathbf{v}_n) d\Omega = (\text{K.E.})_{n+1} - (\text{K.E.})_n. \end{aligned}$$

Combining all the above results, we get from (8) in the absence of loading

$$(\text{K.E.})_n + \hat{W}_n = (\text{K.E.})_{n+1} + \hat{W}_{n+1}, \quad (13)$$

which is the desired result.

Ideally speaking, energy dissipation should be introduced into the numerical algorithm by using an appropriate numerical approximation of the continuum viscoelastic (or viscoelastoplastic) constitutive relation while formulating \mathbf{S}_{alg} . Thus, the algorithmic stress can be taken to be the sum of a conserving part \mathbf{S}_{cons} — as given by (10) — and a dissipative part \mathbf{S}_{diss} which is a numerical approximation of the viscoelastic part, that is, $\mathbf{S}_{\text{alg}} = \mathbf{S}_{\text{cons}} + \mathbf{S}_{\text{diss}}$. For illustrative purposes, we use the Kelvin–Voigt viscoelastic model in this work, which is

$$\mathbf{S}_{\text{diss}} = \frac{\alpha}{t_\Delta} (\bar{\mathbf{E}}_{n+1} - \bar{\mathbf{E}}_n), \quad \alpha > 0.$$

Since $(\bar{\mathbf{E}}_{n+1} - \bar{\mathbf{E}}_n) : (\bar{\mathbf{E}}_{n+1} - \bar{\mathbf{E}}_n) \geq 0$, instead of (13), we now get $(\text{K.E.})_{n+1} + \hat{W}_{n+1} \leq (\text{K.E.})_n + \hat{W}_n$, which shows that the total energy is a nonincreasing function of time. The energy conserving algorithm is recovered simply by setting α to zero. Having an energy dissipation strategy may be important when one is interested simply in the static steady-state solution, say in buckling problems where finding the static solution directly may involve the use of complicated path-following algorithms. In such cases, the use of the exact viscoelastic constitutive model is not needed.

On using (10), we get for a Saint-Venant–Kirchhoff material,

$$\mathbf{S}_{\text{cons}} = \frac{1}{2} (\mathbf{S}_n + \mathbf{S}_{n+1}).$$

For general nonlinear constitutive models, firstly it may be difficult to evaluate \mathbf{S}_{alg} analytically (note that the same problem exists for the single-field formulation also), and secondly even if one is able to analytically find \mathbf{S}_{alg} , in the fully discrete setting, the choice $\mathbf{S}_\delta = \mathbf{S}_{\text{alg}}$ may not lie in the admissible stress space. If we use a trapezoidal approximation for evaluating the integral in (10) (which is a first-order approximation similar to the approximations being made for the velocity and acceleration) for \mathbf{S}_{cons} , meaning $\mathbf{S}_{\text{cons}} = (\mathbf{S}_n + \mathbf{S}_{n+1})/2$, then one can realize the selection $\mathbf{S}_\delta = \mathbf{S}_{\text{alg}}$. As we shall show in Section 4 (see Section 4.7), this turns out to be a good approximation for nonlinear material models. With this approximation, and with the use of (7), (8) and (9) can be written as

$$\begin{aligned} 2 \int_{\Omega} \rho_0 \mathbf{u}_\delta \cdot \left(\frac{\mathbf{u}_{n+1} - \mathbf{u}_n}{t_\Delta^2} - \frac{\mathbf{v}_n}{t_\Delta} \right) d\Omega + \int_{\Omega} \left(\frac{\bar{\mathbf{E}}_\delta)_n + (\bar{\mathbf{E}}_\delta)_{n+1}}{2} \right) : \left(\frac{\mathbf{S}_n + \mathbf{S}_{n+1}}{2} + \frac{\alpha(\bar{\mathbf{E}}_{n+1} - \bar{\mathbf{E}}_n)}{t_\Delta} \right) d\Omega \\ = \int_{\Omega} \rho_0 \mathbf{u}_\delta \cdot \mathbf{b}_{\text{alg}} d\Omega + \int_{\Gamma_t} \mathbf{u}_\delta \cdot \bar{\mathbf{t}}_{\text{alg}} d\Gamma, \quad \forall \mathbf{u}_\delta \in V_u, \quad (14) \end{aligned}$$

$$\int_{\Omega} \mathbf{S}_\delta : [\bar{\mathbf{E}}(\mathbf{u}_{n+1}) - \hat{\mathbf{E}}(\mathbf{S}_{n+1})] d\Omega = 0, \quad \forall \mathbf{S}_\delta \in V_S. \quad (15)$$

3. Linearization and finite element approximation

3.1. Linearization of the variational formulation. With a view towards developing an iterative finite element scheme, we now linearize the variational statements in (14) and (15). For simplicity, we consider the loads to be dead loads (meaning loads that are independent of the deformation \mathbf{u}); the case of live loads such as pressure loading can be treated by using the results in [Jog and Kelkar 2006]. Let the superscripts k and $k+1$ denote the values of the field variables at the k and $(k+1)$ -th iterative steps, and let $(\mathbf{u}_\Delta, \mathbf{S}_\Delta)$ denote the increments in the displacement and stress fields at time t_{n+1} . Then, keeping in view that \mathbf{u} and \mathbf{S} are *independent* field variables, and by an application of the chain and product rules, we have, for example,

$$\begin{aligned} (\mathbf{S} : \bar{\mathbf{E}}_\delta)_{n+1}^{k+1} &\approx (\mathbf{S} : \bar{\mathbf{E}}_\delta)_{n+1}^k + D_u(\mathbf{S} : \bar{\mathbf{E}}_\delta)(\mathbf{u}_{n+1}^k, \mathbf{S}_{n+1}^k)[\mathbf{u}_\Delta] + D_S(\mathbf{S} : \bar{\mathbf{E}}_\delta)(\mathbf{u}_{n+1}^k, \mathbf{S}_{n+1}^k)[\mathbf{S}_\Delta] \\ &= (\mathbf{S} : \bar{\mathbf{E}}_\delta)_{n+1}^k + [(\nabla \mathbf{u}_\delta) \mathbf{S}_{n+1}] : (\nabla \mathbf{u}_\Delta) + \mathbf{S}_\Delta : (\bar{\mathbf{E}}_\delta)_{n+1}, \end{aligned} \quad (16)$$

$$\mathbf{S}_\delta : [\bar{\mathbf{E}}(\mathbf{u}_{n+1}^{k+1}) - \hat{\mathbf{E}}(\mathbf{S}_{n+1}^{k+1})] \approx \mathbf{S}_\delta : [\bar{\mathbf{E}}(\mathbf{u}_{n+1}^k) - \hat{\mathbf{E}}(\mathbf{S}_{n+1}^k)] + \mathbf{S}_\delta : D\bar{\mathbf{E}}(\mathbf{u}_{n+1}^k)[\mathbf{u}_\Delta] - \mathbf{S}_\delta : \mathbb{C}^{-1}[\mathbf{S}_\Delta], \quad (17)$$

where $\mathbb{C}^{-1} = \partial \hat{\mathbf{E}} / \partial \mathbf{S}$ is the (fourth-order) material compliance tensor and

$$D\bar{\mathbf{E}}(\mathbf{u}_{n+1}^k)[\mathbf{u}_\Delta] = \frac{1}{2} [(\nabla \mathbf{u}_\Delta) + (\nabla \mathbf{u}_\Delta)^T + (\nabla \mathbf{u}_{n+1}^k)^T (\nabla \mathbf{u}_\Delta) + (\nabla \mathbf{u}_\Delta)^T (\nabla \mathbf{u}_{n+1}^k)]. \quad (18)$$

The other terms in (14) and (15) are linearized in a similar manner to get the incremental forms of the variational equations.

For a computer implementation, it is convenient to express second-order tensors as vectors and fourth-order tensors as matrices. Hence, we define the engineering strains, stresses, and displacement-increment gradients as

$$\mathbf{E}_c(\mathbf{S}) = \begin{bmatrix} E_{11} \\ E_{22} \\ E_{33} \\ 2E_{12} \\ 2E_{23} \\ 2E_{13} \end{bmatrix}, \quad \bar{\mathbf{E}}_c(\mathbf{u}) = \begin{bmatrix} \bar{E}_{11} \\ \bar{E}_{22} \\ \bar{E}_{33} \\ 2\bar{E}_{12} \\ 2\bar{E}_{23} \\ 2\bar{E}_{13} \end{bmatrix}, \quad \mathbf{S}_c = \begin{bmatrix} S_{11} \\ S_{22} \\ S_{33} \\ S_{12} \\ S_{23} \\ S_{13} \end{bmatrix}, \quad (\nabla \mathbf{u}_\Delta)_c = \begin{bmatrix} (\nabla \mathbf{u}_\Delta)_{11} \\ (\nabla \mathbf{u}_\Delta)_{12} \\ (\nabla \mathbf{u}_\Delta)_{13} \\ (\nabla \mathbf{u}_\Delta)_{21} \\ (\nabla \mathbf{u}_\Delta)_{22} \\ (\nabla \mathbf{u}_\Delta)_{23} \\ (\nabla \mathbf{u}_\Delta)_{31} \\ (\nabla \mathbf{u}_\Delta)_{32} \\ (\nabla \mathbf{u}_\Delta)_{33} \end{bmatrix}, \quad (19)$$

the engineering form of the tensor $D\bar{\mathbf{E}}(\mathbf{u}^k)[\mathbf{u}_\Delta]$ as (with summation over i implied)

$$\{D\bar{\mathbf{E}}(\mathbf{u}_{n+1}^k)[\mathbf{u}_\Delta]\}_c = \begin{bmatrix} (\nabla \mathbf{u}_\Delta)_{11} + (\nabla \mathbf{u}_{n+1}^k)_{i1}(\nabla \mathbf{u}_\Delta)_{i1} \\ (\nabla \mathbf{u}_\Delta)_{22} + (\nabla \mathbf{u}_{n+1}^k)_{i2}(\nabla \mathbf{u}_\Delta)_{i2} \\ (\nabla \mathbf{u}_\Delta)_{33} + (\nabla \mathbf{u}_{n+1}^k)_{i3}(\nabla \mathbf{u}_\Delta)_{i3} \\ (\nabla \mathbf{u}_\Delta)_{12} + (\nabla \mathbf{u}_\Delta)_{21} + (\nabla \mathbf{u}_{n+1}^k)_{i1}(\nabla \mathbf{u}_\Delta)_{i2} + (\nabla \mathbf{u}_{n+1}^k)_{i2}(\nabla \mathbf{u}_\Delta)_{i1} \\ (\nabla \mathbf{u}_\Delta)_{23} + (\nabla \mathbf{u}_\Delta)_{32} + (\nabla \mathbf{u}_{n+1}^k)_{i2}(\nabla \mathbf{u}_\Delta)_{i3} + (\nabla \mathbf{u}_{n+1}^k)_{i3}(\nabla \mathbf{u}_\Delta)_{i2} \\ (\nabla \mathbf{u}_\Delta)_{13} + (\nabla \mathbf{u}_\Delta)_{31} + (\nabla \mathbf{u}_{n+1}^k)_{i1}(\nabla \mathbf{u}_\Delta)_{i3} + (\nabla \mathbf{u}_{n+1}^k)_{i3}(\nabla \mathbf{u}_\Delta)_{i1} \end{bmatrix}, \quad (20)$$

the stress matrix as

$$\mathbf{S}_M = \begin{bmatrix} S_{11} & S_{12} & S_{13} & 0 & 0 & 0 & 0 & 0 & 0 \\ S_{12} & S_{22} & S_{23} & 0 & 0 & 0 & 0 & 0 & 0 \\ S_{31} & S_{32} & S_{33} & 0 & 0 & 0 & 0 & 0 & 0 \\ 0 & 0 & 0 & S_{11} & S_{12} & S_{13} & 0 & 0 & 0 \\ 0 & 0 & 0 & S_{12} & S_{22} & S_{23} & 0 & 0 & 0 \\ 0 & 0 & 0 & S_{31} & S_{32} & S_{33} & 0 & 0 & 0 \\ 0 & 0 & 0 & 0 & 0 & 0 & S_{11} & S_{12} & S_{13} \\ 0 & 0 & 0 & 0 & 0 & 0 & S_{12} & S_{22} & S_{23} \\ 0 & 0 & 0 & 0 & 0 & 0 & S_{31} & S_{32} & S_{33} \end{bmatrix}, \quad (21)$$

and the engineering form of the material constitutive tensor as

$$\mathbb{C}_c = \begin{bmatrix} C_{1111} & C_{1122} & C_{1133} & C_{1112} & C_{1123} & C_{1113} \\ C_{2211} & C_{2222} & C_{2233} & C_{2212} & C_{2223} & C_{2213} \\ C_{3311} & C_{3322} & C_{3333} & C_{3312} & C_{3323} & C_{3313} \\ C_{1211} & C_{1222} & C_{1233} & C_{1212} & C_{1223} & C_{1213} \\ C_{2311} & C_{2322} & C_{2333} & C_{2312} & C_{2323} & C_{2313} \\ C_{1311} & C_{1322} & C_{1333} & C_{1312} & C_{1323} & C_{1313} \end{bmatrix}. \quad (22)$$

Note that $[\bar{\mathbf{E}}_\delta(\mathbf{u}_{n+1}^k)]_c = \{D\bar{\mathbf{E}}(\mathbf{u}_{n+1}^k)[\mathbf{u}_\delta]\}_c$, where \mathbf{u}_δ is the variation of \mathbf{u} .

In terms of these engineering quantities, the incremental form of the variational statements (14) and (15) is

$$\begin{aligned} & \frac{2}{t_\Delta^2} \int_\Omega \rho_0 \mathbf{u}_\delta^T \mathbf{u}_\Delta d\Omega \\ & + \frac{1}{4} \int_\Omega \left((\nabla \mathbf{u}_\delta)_c^T \left[\mathbf{S}_n + \mathbf{S}_{n+1}^k + \frac{2\alpha}{t_\Delta} (\bar{\mathbf{E}}_{n+1}^k - \bar{\mathbf{E}}_n) \right]_M (\nabla \mathbf{u}_\Delta)_c \right. \\ & \quad \left. + [D\bar{\mathbf{E}}(\mathbf{u}_n + \mathbf{u}_{n+1}^k)[\mathbf{u}_\delta]]_c^T \left[(\mathbf{S}_\Delta)_c + \frac{2\alpha}{t_\Delta} [D\bar{\mathbf{E}}(\mathbf{u}_{n+1}^k)[\mathbf{u}_\Delta]]_c \right] \right) d\Omega \\ & = \int_\Omega \rho_0 \mathbf{u}_\delta^T \mathbf{b}_{\text{alg}} d\Omega + \int_{\Gamma_i} \mathbf{u}_\delta^T \bar{\mathbf{t}}_{\text{alg}} d\Gamma - 2 \int_\Omega \rho_0 \mathbf{u}_\delta^T \left(\frac{\mathbf{u}_{n+1}^k - \mathbf{u}_n}{t_\Delta^2} - \frac{\mathbf{v}_n}{t_\Delta} \right) \\ & \quad - \frac{1}{4} \int_\Omega [D\bar{\mathbf{E}}(\mathbf{u}_n + \mathbf{u}_{n+1}^k)[\mathbf{u}_\delta]]_c^T \left[(\mathbf{S}_n)_c + (\mathbf{S}_{n+1}^k)_c + \frac{2\alpha}{t_\Delta} [(\bar{\mathbf{E}}_{n+1}^k)_c - (\bar{\mathbf{E}}_n)_c] \right] d\Omega, \quad \forall \mathbf{u}_\delta \in V_u, \quad (23) \end{aligned}$$

$$\begin{aligned} & \int_\Omega (\mathbf{S}_\delta)_c^T [D\bar{\mathbf{E}}(\mathbf{u}_{n+1}^k)[\mathbf{u}_\Delta]]_c d\Omega - \int_\Omega (\mathbf{S}_\delta)_c^T \mathbb{C}_c^{-1} (\mathbf{S}_\Delta)_c d\Omega \\ & = \int_\Omega (\mathbf{S}_\delta)_c^T [\hat{\mathbf{E}}_c(\mathbf{S}_{n+1}^k) - \bar{\mathbf{E}}_c(\mathbf{u}_{n+1}^k)] d\Omega, \quad \forall \mathbf{S}_\delta \in V_S. \quad (24) \end{aligned}$$

3.2. Finite element discretization. To obtain the finite element matrices, we introduce the discretizations

$$\mathbf{u} = \mathbf{N}\hat{\mathbf{u}}, \quad \mathbf{u}_\delta = \mathbf{N}\hat{\mathbf{u}}_\delta, \quad \mathbf{u}_\Delta = \mathbf{N}\hat{\mathbf{u}}_\Delta, \quad \mathbf{S}_c = \mathbf{P}\boldsymbol{\beta}, \quad (\mathbf{S}_\delta)_c = \mathbf{P}\boldsymbol{\beta}_\delta, \quad (\mathbf{S}_\Delta)_c = \mathbf{P}\boldsymbol{\beta}_\Delta. \quad (25)$$

The shape functions \mathbf{N} are the standard isoparametric displacement shape functions. The choice of the stress interpolation functions \mathbf{P} is discussed in Section 3.3. Using these interpolations, we have

$$\begin{aligned} \{D\bar{\mathbf{E}}(\mathbf{u}_{n+1}^k)[\mathbf{u}_\Delta]\}_c &= (\mathbf{B}_L)_{n+1} \hat{\mathbf{u}}_\Delta, & (\nabla \mathbf{u}_\Delta)_c &= \mathbf{B}_{NL} \hat{\mathbf{u}}_\Delta, \\ \{D\bar{\mathbf{E}}(\mathbf{u}_{n+1}^k)[\mathbf{u}_\delta]\}_c &= (\mathbf{B}_L)_{n+1} \hat{\mathbf{u}}_\delta, & (\nabla \mathbf{u}_\delta)_c &= \mathbf{B}_{NL} \hat{\mathbf{u}}_\delta, \end{aligned}$$

where $(\mathbf{B}_L)_{n+1} = \mathbf{B}_{L1} + \mathbf{B}_{L2}$, with

$$\mathbf{B}_{L1} = \begin{bmatrix} N_{1,1} & 0 & 0 & N_{2,1} & 0 & 0 & \dots \\ 0 & N_{1,2} & 0 & 0 & N_{2,2} & 0 & \dots \\ 0 & 0 & N_{1,3} & 0 & 0 & N_{2,3} & \dots \\ N_{1,2} & N_{1,1} & 0 & N_{2,2} & N_{2,1} & 0 & \dots \\ 0 & N_{1,3} & N_{1,2} & 0 & N_{2,3} & N_{2,2} & \dots \\ N_{1,3} & 0 & N_{1,1} & N_{2,3} & 0 & N_{2,1} & \dots \end{bmatrix},$$

$$\mathbf{B}_{L2} = \begin{bmatrix} (\nabla \mathbf{u}_{n+1}^k)_{11} N_{1,1} & (\nabla \mathbf{u}_{n+1}^k)_{21} N_{1,1} & (\nabla \mathbf{u}_{n+1}^k)_{31} N_{1,1} & \dots \\ (\nabla \mathbf{u}_{n+1}^k)_{12} N_{1,2} & (\nabla \mathbf{u}_{n+1}^k)_{22} N_{1,2} & (\nabla \mathbf{u}_{n+1}^k)_{32} N_{1,2} & \dots \\ (\nabla \mathbf{u}_{n+1}^k)_{13} N_{1,3} & (\nabla \mathbf{u}_{n+1}^k)_{23} N_{1,3} & (\nabla \mathbf{u}_{n+1}^k)_{33} N_{1,3} & \dots \\ (\nabla \mathbf{u}_{n+1}^k)_{12} N_{1,1} + (\nabla \mathbf{u}_{n+1}^k)_{11} N_{1,2} & (\nabla \mathbf{u}_{n+1}^k)_{22} N_{1,1} + (\nabla \mathbf{u}_{n+1}^k)_{21} N_{1,2} & (\nabla \mathbf{u}_{n+1}^k)_{32} N_{1,1} + (\nabla \mathbf{u}_{n+1}^k)_{31} N_{1,2} & \dots \\ (\nabla \mathbf{u}_{n+1}^k)_{13} N_{1,2} + (\nabla \mathbf{u}_{n+1}^k)_{12} N_{1,3} & (\nabla \mathbf{u}_{n+1}^k)_{23} N_{1,2} + (\nabla \mathbf{u}_{n+1}^k)_{22} N_{1,3} & (\nabla \mathbf{u}_{n+1}^k)_{33} N_{1,2} + (\nabla \mathbf{u}_{n+1}^k)_{32} N_{1,3} & \dots \\ (\nabla \mathbf{u}_{n+1}^k)_{11} N_{1,3} + (\nabla \mathbf{u}_{n+1}^k)_{13} N_{1,1} & (\nabla \mathbf{u}_{n+1}^k)_{21} N_{1,3} + (\nabla \mathbf{u}_{n+1}^k)_{23} N_{1,1} & (\nabla \mathbf{u}_{n+1}^k)_{31} N_{1,3} + (\nabla \mathbf{u}_{n+1}^k)_{33} N_{1,1} & \dots \end{bmatrix},$$

$$\mathbf{B}_{NL} = \begin{bmatrix} N_{1,1} & 0 & 0 & N_{2,1} & 0 & 0 & \dots \\ N_{1,2} & 0 & 0 & N_{2,2} & 0 & 0 & \dots \\ N_{1,3} & 0 & 0 & N_{2,3} & 0 & 0 & \dots \\ 0 & N_{1,1} & 0 & 0 & N_{2,1} & 0 & \dots \\ 0 & N_{1,2} & 0 & 0 & N_{2,2} & 0 & \dots \\ 0 & N_{1,3} & 0 & 0 & N_{2,3} & 0 & \dots \\ 0 & 0 & N_{1,1} & 0 & 0 & N_{2,1} & \dots \\ 0 & 0 & N_{1,2} & 0 & 0 & N_{2,2} & \dots \\ 0 & 0 & N_{1,3} & 0 & 0 & N_{2,3} & \dots \end{bmatrix}.$$

Let $\mathbf{M} := \int_{\Omega} \rho_0 \mathbf{N}^T \mathbf{N} d\Omega$. Using the arbitrariness of $\hat{\mathbf{u}}_{\delta}$ and $\boldsymbol{\beta}_{\delta}$, the matrix form of the incremental equations (23) and (24) can be written as

$$\mathbf{Q}\hat{\mathbf{u}}_{\Delta} + \mathbf{G}_1^T \boldsymbol{\beta}_{\Delta} = \mathbf{f}_1, \quad \mathbf{G}_2 \hat{\mathbf{u}}_{\Delta} - \mathbf{H} \boldsymbol{\beta}_{\Delta} = \mathbf{f}_2, \quad (26)$$

where

$$\begin{aligned} \mathbf{Q} &= \frac{2\mathbf{M}}{t_{\Delta}^2} + \frac{1}{4} \int_{\Omega} \mathbf{B}_{NL}^T \left[\mathbf{S}_n + \mathbf{S}_{n+1}^k + \frac{2\alpha}{t_{\Delta}} (\bar{\mathbf{E}}_{n+1}^k - \bar{\mathbf{E}}_n) \right]_M \mathbf{B}_{NL} d\Omega + \frac{\alpha}{2t_{\Delta}} \int_{\Omega_e} [(\mathbf{B}_L)_n + (\mathbf{B}_L)_{n+1}^k]^T (\mathbf{B}_L)_{n+1}^k d\Omega, \\ \mathbf{G}_1 &= \frac{1}{4} \int_{\Omega} \mathbf{P}^T [(\mathbf{B}_L)_n + (\mathbf{B}_L)_{n+1}^k] d\Omega, \\ \mathbf{G}_2 &= \int_{\Omega} \mathbf{P}^T (\mathbf{B}_L)_{n+1}^k d\Omega, \\ \mathbf{H} &= \int_{\Omega} \mathbf{P}^T \mathbb{C}_c^{-1} \mathbf{P} d\Omega, \\ \mathbf{f}_1 &= \int_{\Omega} \rho_0 \mathbf{N}^T \mathbf{b}_{\text{alg}} d\Omega + \int_{\Gamma_i} \mathbf{N}^T \bar{\mathbf{t}}_{\text{alg}} d\Gamma - \frac{1}{4} \int_{\Omega} [(\mathbf{B}_L)_n + (\mathbf{B}_L)_{n+1}^k]^T \left[\mathbf{S}_n + \mathbf{S}_{n+1}^k + \frac{2\alpha}{t_{\Delta}} [\bar{\mathbf{E}}_{n+1}^k - \bar{\mathbf{E}}_n] \right]_c d\Omega \\ &\quad - \frac{2}{t_{\Delta}^2} \int_{\Omega} \rho_0 \mathbf{N}^T (\mathbf{u}_{n+1}^k - \mathbf{u}_n) d\Omega + \frac{2}{t_{\Delta}} \int_{\Omega} \rho_0 \mathbf{N}^T \mathbf{v}_n d\Omega, \\ \mathbf{f}_2 &= \int_{\Omega} \mathbf{P}^T [\hat{\mathbf{E}}_c(\mathbf{S}_{n+1}^k) - \bar{\mathbf{E}}_c(\mathbf{u}_{n+1}^k)] d\Omega. \end{aligned} \quad (27)$$

Eliminating $\boldsymbol{\beta}_{\Delta}$ in (26), we get

$$\mathbf{K} \hat{\mathbf{u}}_{\Delta} = \mathbf{f}_{\Delta}, \quad (28)$$

where

$$\mathbf{K} = \mathbf{Q} + \mathbf{G}_1^T \mathbf{H}^{-1} \mathbf{G}_2 \quad \text{and} \quad \mathbf{f}_{\Delta} = \mathbf{f}_1 + \mathbf{G}_1^T \mathbf{H}^{-1} \mathbf{f}_2. \quad (29)$$

Due to the presence of the mass matrix \mathbf{M} , the stiffness matrix \mathbf{K} does not become singular even in dynamic buckling problems, circumventing the need for special strategies such as arc-length methods that are needed to find the load-deflection curve within the static framework.

Since the stress interpolation is allowed to be discontinuous across element boundaries, \mathbf{H}^{-1} is composed of distinct block matrices $\mathbf{H}_{(e)}^{-1}$ associated with each element. Thus, the element stiffness matrix

is given by

$$\mathbf{K}_{(e)} = \mathbf{Q}_{(e)} + (\mathbf{G}_{(e)})_1^T \mathbf{H}_{(e)}^{-1} (\mathbf{G}_{(e)})_2,$$

where, the subscript e indicates that the integrations in Equations (27) are carried out over the element domain Ω_e instead of over Ω . Once \mathbf{u}_Δ is obtained from (28), the stresses are updated using $\mathbf{S}_c^{k+1} = \mathbf{S}_c^k + (\mathbf{S}_\Delta)_c$, where

$$(\mathbf{S}_\Delta)_c^{(e)} = \mathbf{P}_{(e)}(\boldsymbol{\beta}_\Delta)_{(e)} = \mathbf{P}_{(e)} \mathbf{H}_{(e)}^{-1} [\mathbf{G}_2 \mathbf{u}_\Delta - \mathbf{f}_2]_{(e)},$$

and, finally, the strains \mathbf{E}^{k+1} are obtained using the constitutive relation $\mathbf{S}^{k+1} = \hat{\mathbf{S}}(\mathbf{E}^{k+1})$. The velocity field \mathbf{v}_{n+1} is recovered using (7).

In a standard displacement-based isoparametric formulation, the stiffness matrix is given by

$$\mathbf{K}_{(e)}^{\text{disp}} = \mathbf{Q}_{(e)} + \frac{1}{4} \int_{\Omega_e} [(\mathbf{B}_L)_n + (\mathbf{B}_L)_{n+1}^k]^T \mathbb{C}_c (\mathbf{B}_L)_{n+1}^k d\Omega, \quad (30)$$

while \mathbf{f}_Δ is simply given by \mathbf{f}_1 . Thus, the difference between the displacement-based and hybrid stiffness matrices is in the second term, similar to the static case. As we shall see in Section 4, this difference is critical in ensuring that the hybrid elements perform much better compared to displacement-based elements.

3.3. Choice of the stress interpolation function. For the 8-node hexahedral element, we use the stress interpolation given in [Pian and Tong 1986; Sze and Fan 1996], while for the 4-node axisymmetric element, we use the stress interpolation in [Jog and Annabattula 2006], which uses the same in-plane stress interpolation as the Pian–Sumihara 4-node quadrilateral element [Pian and Sumihara 1984]. These elements satisfy the inf-sup conditions [Xue et al. 1985].

Lee and Rhiu [1986] have developed a procedure for finding the stress interpolation for a 9-node planar quadrilateral element which leads to

$$\begin{aligned} S^{\zeta\zeta} &= \beta_1 + \beta_2\zeta + \beta_3\eta + \beta_4\zeta\eta + \beta_{13}\zeta\eta^2, \\ S^{\eta\eta} &= \beta_5 + \beta_6\zeta + \beta_7\eta + \beta_8\zeta\eta + \beta_{14}\zeta^2\eta, \\ S^{\zeta\eta} &= \beta_9 + \beta_{10}\zeta + \beta_{11}\eta + \beta_{12}\zeta\eta. \end{aligned}$$

The terms η^2 and ζ^2 are excluded from the interpolations for $S^{\zeta\zeta}$ and $S^{\eta\eta}$, respectively, since their exclusion gives rise to a zero-energy mode that is noncommunicable, and hence harmless. Although the above interpolation works extremely well for statics problems, we have found that when used within the context of a 9-node axisymmetric element, the exclusion of these terms causes an instability in the solution of the bar-impact problem discussed in Section 4.5. When the interpolation is modified so as to include these terms, meaning when we use

$$\begin{aligned} S^{\zeta\zeta} &= \beta_1 + \beta_2\zeta + \beta_3\eta + \beta_4\zeta\eta + \beta_5\eta^2 + \beta_6\zeta\eta^2, & S^{\zeta\eta} &= \beta_{13} + \beta_{14}\zeta + \beta_{15}\eta + \beta_{16}\zeta\eta, \\ S^{\eta\eta} &= \beta_7 + \beta_8\zeta + \beta_9\eta + \beta_{10}\zeta\eta + \beta_{11}\zeta^2 + \beta_{12}\zeta^2\eta, & S^{\theta\theta} &= \beta_{17} + \beta_{18}\zeta + \beta_{19}\eta + \beta_{20}\zeta\eta, \end{aligned} \quad (31)$$

the instability no longer occurs. One could also use an interpolation of the form

$$\begin{aligned} S^{\zeta\zeta} &= \beta_1 + \beta_2\zeta + \beta_3\eta + \beta_4\zeta\eta + \beta_5\eta^2 + \beta_6\zeta\eta^2, & S^{\zeta\eta} &= \beta_{13} + \beta_{14}\zeta + \beta_{15}\eta, \\ S^{\eta\eta} &= \beta_7 + \beta_8\zeta + \beta_9\eta + \beta_{10}\zeta\eta + \beta_{11}\zeta^2 + \beta_{12}\zeta^2\eta, & S^{\theta\theta} &= \beta_{16} + (J_{12}\zeta + J_{22}\eta)\beta_{17}, \end{aligned}$$

where J_{12} and J_{22} denote entries of the Jacobian matrix as in [Jog and Annabattula 2006]; this has the same normal stress interpolation as (31), it uses the minimum number of β parameters, and results in a full-rank stiffness matrix (apart from rigid-body modes). However, the exclusion of lower-order terms from the $S^{\xi\eta}$ and $S^{\theta\theta}$ interpolations leads to bad results even on statics problems. Thus, although the 20β model does result in a slight stiffening compared to the 17β model of [Jog and Annabattula 2006], it is more robust within the framework of transient problems. Of course, since a static solution can be considered to be steady-state solution of a transient problem, one should use the 20β model within the static framework also.

In a similar manner, for the 27-node hexahedral element developed in [Jog 2005], one now uses a normal stress interpolation that is obtained by differentiating the displacement interpolation field. Leaving out some terms may result in a full-rank stiffness matrix and may yield extremely good results on statics problems, as shown in [Jog 2005], but results in the same instability as mentioned above in the bar-impact problem. Carrying out this modification, we now use the following interpolation:

$$\begin{aligned}
S^{\xi\xi} &= \beta_1 + \beta_2\xi + \beta_3\eta + \beta_4\zeta + \beta_5\xi\eta + \beta_6\eta\zeta + \beta_7\xi\zeta + \beta_8\xi\eta\zeta + \beta_9\xi\eta^2 + \beta_{10}\xi\zeta^2 \\
&\quad + \beta_{11}\xi\eta\zeta^2 + \beta_{12}\xi\eta^2\zeta + \beta_{13}\xi\eta^2\zeta^2 + \beta_{14}\eta^2 + \beta_{15}\zeta^2 + \beta_{16}\eta^2\zeta + \beta_{17}\eta\zeta^2 + \beta_{18}\eta^2\zeta^2, \\
S^{\eta\eta} &= \beta_{19} + \beta_{20}\xi + \beta_{21}\eta + \beta_{22}\zeta + \beta_{23}\xi\eta + \beta_{24}\eta\zeta + \beta_{25}\xi\zeta + \beta_{26}\xi\eta\zeta + \beta_{27}\xi^2\eta + \beta_{28}\eta\zeta^2 \\
&\quad + \beta_{29}\xi^2\eta\zeta + \beta_{30}\xi\eta\zeta^2 + \beta_{31}\xi^2\eta\zeta^2 + \beta_{32}\xi^2 + \beta_{33}\zeta^2 + \beta_{34}\xi^2\zeta + \beta_{35}\xi\zeta^2 + \beta_{36}\xi^2\zeta^2, \\
S^{\zeta\zeta} &= \beta_{37} + \beta_{38}\xi + \beta_{39}\eta + \beta_{40}\zeta + \beta_{41}\xi\eta + \beta_{42}\eta\zeta + \beta_{43}\xi\zeta + \beta_{44}\xi\eta\zeta + \beta_{45}\xi^2\zeta + \beta_{46}\eta^2\zeta \\
&\quad + \beta_{47}\xi^2\eta\zeta + \beta_{48}\xi\eta^2\zeta + \beta_{49}\xi^2\eta^2\zeta + \beta_{50}\xi^2 + \beta_{51}\eta^2 + \beta_{52}\xi^2\eta + \beta_{53}\xi\eta^2 + \beta_{54}\xi^2\eta^2, \\
S^{\xi\eta} &= \beta_{55} + \beta_{56}\xi + \beta_{57}\eta + \beta_{58}\zeta + \beta_{59}\xi\eta + \beta_{60}\eta\zeta + \beta_{61}\xi\zeta + \beta_{62}\xi\eta\zeta + \beta_{63}\xi\zeta^2 + \beta_{64}\eta\zeta^2, \\
S^{\eta\zeta} &= \beta_{65} + \beta_{66}\xi + \beta_{67}\eta + \beta_{68}\zeta + \beta_{69}\xi\eta + \beta_{70}\eta\zeta + \beta_{71}\xi\zeta + \beta_{72}\xi\eta\zeta + \beta_{73}\xi^2\eta + \beta_{74}\xi^2\zeta, \\
S^{\xi\zeta} &= \beta_{75} + \beta_{76}\xi + \beta_{77}\eta + \beta_{78}\zeta + \beta_{79}\xi\eta + \beta_{80}\eta\zeta + \beta_{81}\xi\zeta + \beta_{82}\xi\eta\zeta + \beta_{83}\xi\eta^2 + \beta_{84}\eta^2\zeta. \tag{32}
\end{aligned}$$

The zero-energy modes that were earlier suppressed by the terms $\xi\eta\zeta^2$, $\xi^2\eta\zeta$, and $\xi\eta^2\zeta$ in the $S^{\xi\eta}$, $S^{\eta\zeta}$, and $S^{\xi\zeta}$ interpolations are now suppressed due to the inclusion of the terms $\eta^2\zeta^2$, $\xi^2\zeta^2$, and $\xi^2\eta^2$ in the $S^{\xi\xi}$, $S^{\eta\eta}$, and $S^{\zeta\zeta}$ interpolations, and hence these terms are excluded from the shear interpolation.

Similarly to the axisymmetric case, one could develop a 75β element, which has the same normal stress interpolation as above and which results in a full-rank stiffness matrix, as follows:

$$\begin{aligned}
S^{\xi\xi} &= \beta_1 + \beta_2\xi + \beta_3\eta + \beta_4\zeta + \beta_5\xi\eta + \beta_6\eta\zeta + \beta_7\xi\zeta + \beta_8\xi\eta\zeta + \beta_9\xi\eta^2 + \beta_{10}\xi\zeta^2 \\
&\quad + \beta_{11}\xi\eta\zeta^2 + \beta_{12}\xi\eta^2\zeta + \beta_{13}\xi\eta^2\zeta^2 + \beta_{14}\eta^2 + \beta_{15}\zeta^2 + \beta_{16}\eta^2\zeta + \beta_{17}\eta\zeta^2 + \beta_{18}\eta^2\zeta^2, \\
S^{\eta\eta} &= \beta_{19} + \beta_{20}\xi + \beta_{21}\eta + \beta_{22}\zeta + \beta_{23}\xi\eta + \beta_{24}\eta\zeta + \beta_{25}\xi\zeta + \beta_{26}\xi\eta\zeta + \beta_{27}\xi^2\eta + \beta_{28}\eta\zeta^2 \\
&\quad + \beta_{29}\xi^2\eta\zeta + \beta_{30}\xi\eta\zeta^2 + \beta_{31}\xi^2\eta\zeta^2 + \beta_{32}\xi^2 + \beta_{33}\zeta^2 + \beta_{34}\xi^2\zeta + \beta_{35}\xi\zeta^2 + \beta_{36}\xi^2\zeta^2, \\
S^{\zeta\zeta} &= \beta_{37} + \beta_{38}\xi + \beta_{39}\eta + \beta_{40}\zeta + \beta_{41}\xi\eta + \beta_{42}\eta\zeta + \beta_{43}\xi\zeta + \beta_{44}\xi\eta\zeta + \beta_{45}\xi^2\zeta + \beta_{46}\eta^2\zeta \\
&\quad + \beta_{47}\xi^2\eta\zeta + \beta_{48}\xi\eta^2\zeta + \beta_{49}\xi^2\eta^2\zeta + \beta_{50}\xi^2 + \beta_{51}\eta^2 + \beta_{52}\xi^2\eta + \beta_{53}\xi\eta^2 + \beta_{54}\xi^2\eta^2, \\
S^{\xi\eta} &= \beta_{55} + \beta_{56}\xi + \beta_{57}\eta + \beta_{58}\zeta + \beta_{59}\xi\eta + \beta_{60}\eta\zeta + \beta_{61}\xi\zeta + \beta_{62}\xi\eta\zeta + \beta_{63}\xi\zeta^2 + \beta_{64}\eta\zeta^2, \\
S^{\eta\zeta} &= \beta_{61} + \beta_{62}\xi + \beta_{63}\eta + \beta_{64}\zeta + \beta_{65}\xi\eta + \beta_{66}\xi\zeta + \beta_{67}\xi\eta\zeta + \beta_{68}\xi^2\zeta + \beta_{69}\xi^2\eta,
\end{aligned}$$

$$S^{\xi\zeta} = \beta_{67} + \beta_{68}\xi + \beta_{69}\eta + \beta_{70}\zeta + \beta_{71}\xi\eta + \beta_{72}\eta\zeta + \beta_{73}\eta^2\zeta + \beta_{75}\xi\eta^2.$$

However, again, the exclusion of lower-order terms from the shear interpolation results in bad performance even on statics problems, and hence the 84β interpolation given by (32) is recommended for both statics and transient problems in view of its increased robustness in transient problems.

Note that the (numerical) instability problem discussed above does not arise in the case of lower-order elements since there the normal stress interpolation is already consistent with the one obtained by differentiating the displacement field.

4. Numerical examples

In this section, we present a wide variety of example problems, ranging from almost rigid to highly flexible beam or shell-type structures, to show the high accuracy and convergence rate of the proposed formulation. We shall denote the energy-momentum conserving displacement-based 27-node and the hybrid 8 and 27-node elements by I27, H8, and H27, respectively. Comparisons are carried out with different strategies presented in the literature by using coarser or equivalent meshes in the space domain, and by using larger or equivalent time steps in the time domain.

As in [Jog and Kelkar 2006], in order to ensure a fair comparison of the results between the I27, H8, and H27 elements, meshes with the *same number of global degrees of freedom* are used. For instance, results obtained using $8N$ H8 elements are compared against the results obtained using N H27 (or I27) elements, with identical nodal coordinate data and boundary conditions used in both meshes. For shell-type problems, one H27/I27 element and two H8 elements are used along the thickness direction. Uniform meshes and time steps are used in all the examples. Full integration is used to evaluate all the integrals arising in the formulation of the elements, and the WSMP sparse matrix solver [Gupta 2000; 2002] is used to solve the system of equations. A Saint-Venant–Kirchhoff material model is used in all the examples unless otherwise stated.

4.1. Flexible bar pendulum under gravity effect. This example was considered in [Yakoub and Shabana 2001]. A bar of length $l = 1$ m and uniform square cross-section (whose dimension is stated in each of the subcases), pinned at one end, oscillates under the effect of gravity, as shown in Figure 1. The bar is released at time $t = 0$ with initial velocity zero from a position $\theta = 90^\circ$. The gravitational acceleration g , the density of the bar ρ_0 , and the Poisson’s ratio are taken to be 9.81 m/s^2 , 7200 kg/m^3 , and 0.3 , respectively. We consider three cases, wherein for the first case, we start with an almost rigid pendulum,

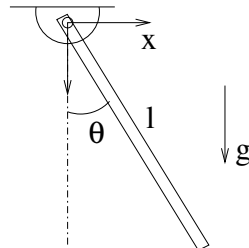


Figure 1. Geometry of the pendulum.

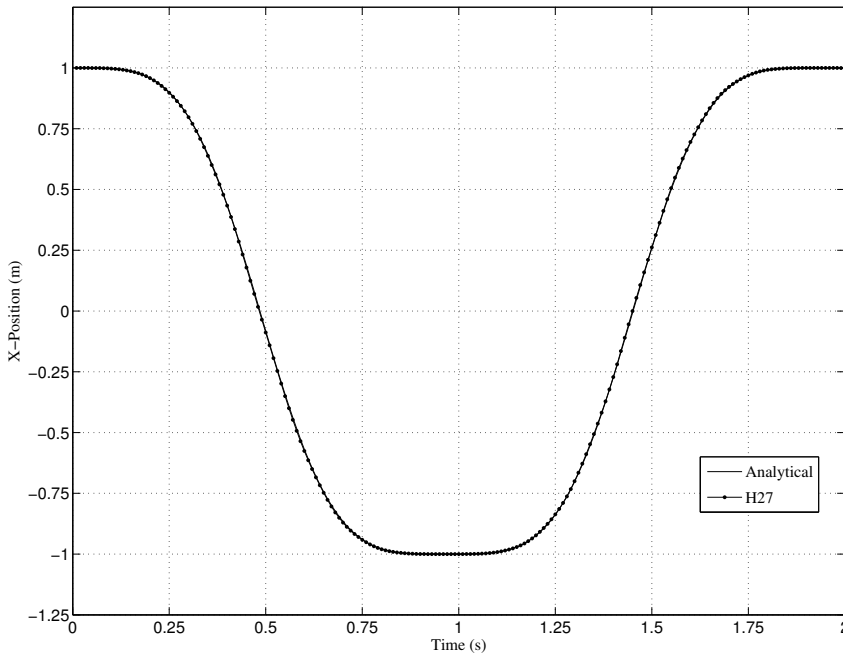


Figure 2. Comparison of the numerically obtained tip displacement of the pendulum with the analytical solution under [Case I](#).

and successively increase its flexibility in the next two cases. Consistent with the theory, the total energy (kinetic, strain, and potential) is obtained to be a constant in all the three cases.

Case I. The Young's modulus E and the cross-section dimension are taken to be 2×10^9 N/m² and 0.02 m, respectively. We use meshes of one H27 and I27 element, and an equivalent mesh for the H8 element. The simulation is carried out over the time interval $[0, 2]$ seconds with $t_{\Delta} = 0.05$ s. Since the flexural rigidity EI is quite high, the motion is almost rigid, and hence we compare our solution with the analytical solution for a rigid bar pendulum given by

$$\theta(t) = 2 \sin^{-1} \left[\frac{1}{\sqrt{2}} \operatorname{sn} \left(\sqrt{\frac{3g}{2l}} t, \frac{1}{\sqrt{2}} \right) \right],$$

where $\operatorname{sn}(\cdot, \cdot)$ denotes the elliptic sine function. As can be seen from [Figure 2](#), there is an almost perfect match between the numerically and analytically obtained solutions. [Yakoub and Shabana \[2001, Figure 6\]](#) also obtain an almost identical solution with 4 elements (the time step is not stated).

A comparison of the iterations taken by the H27 and I27 elements is shown in [Figure 3](#). It is evident that the number of iterations taken by the hybrid element is quite lower.

Case II. The Young's modulus E is decreased to a value 2×10^7 N/m², while the cross-section dimensions is kept the same. Four H27/I27 elements are used to discretize this flexible pendulum. A time step $t_{\Delta} = 0.01$ s is used. The x position of the tip of the pendulum obtained using H27/I27 elements is shown in [Figure 4](#). Eight I27 elements are required to get the same solution as obtained using four H27 elements. The coarse-mesh results of the H27 element match exactly with the ANSYS results presented

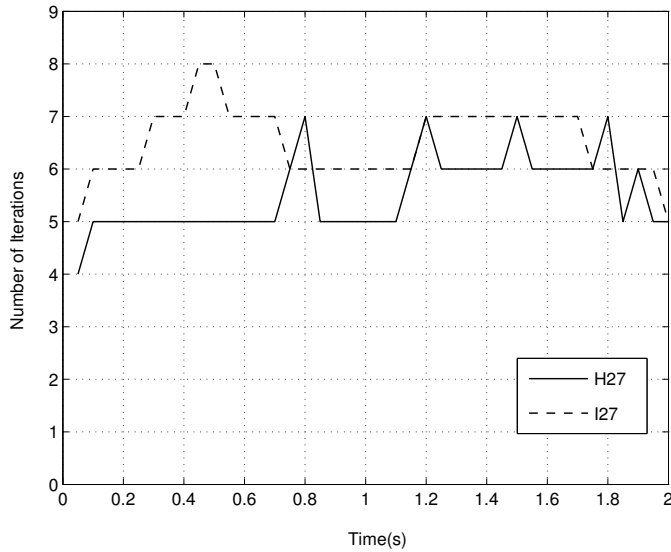


Figure 3. Comparison of the number of iterations taken by the H27 and I27 elements under [Case I](#).

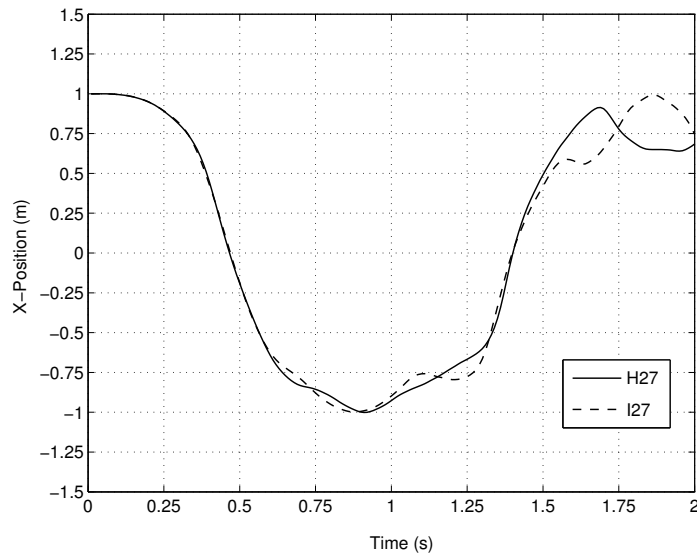


Figure 4. Tip displacement obtained using the H27 and I27 elements under [Case II](#).

in [Yakoub and Shabana 2001, Figure 7]. [Figure 5](#) shows the time history of the transverse deflection of the midpoint of the pendulum from the line joining the two ends of the pendulum, and again shows the substantial difference between the results obtained by the H27 (which match almost perfectly with the ANSYS results shown in [Yakoub and Shabana 2001, Figure 8]) and I27 elements.

Case III. The Young's modulus is maintained at the same value as in [Case II](#), but the cross-section dimension is reduced to 0.01 m. Eight H27/I27 elements are used to discretize the pendulum and the

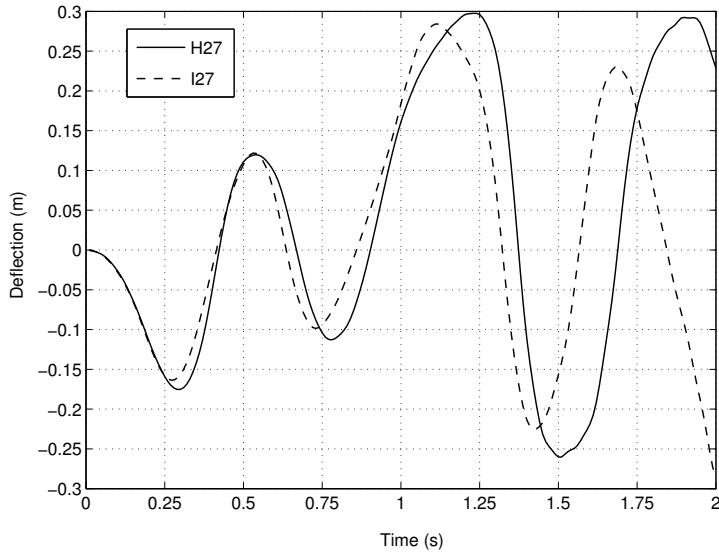


Figure 5. Deflection of the midpoint of the pendulum obtained using the H27 and I27 elements under **Case II**.

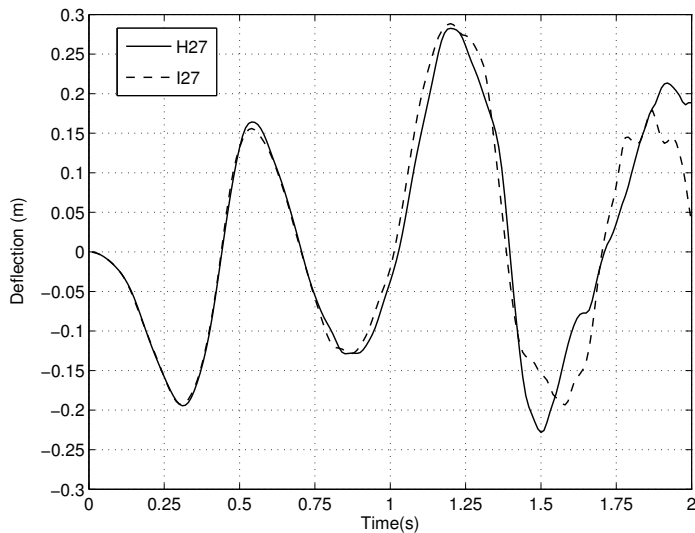


Figure 6. Deflection of the midpoint of the pendulum obtained using the H27 and I27 elements under **Case III**.

time step used is $t_{\Delta} = 0.01$ s. Once again there is a very good agreement between the H27 results shown in [Figure 6](#) and the ANSYS results presented in [\[Yakoub and Shabana 2001, Figure 11\]](#).

4.2. Double pendulum under gravity effect. This example, which has been proposed in [\[Cuadrado et al. 2001\]](#), shows the performance of the algorithm in the case of rigid body motion with multiple links. The double pendulum chosen for study has two identical links of length 1.5 m, and uniform rectangular cross-section of width 0.018973 m and height 0.0632455 m. The acceleration due to gravity g , the Young's

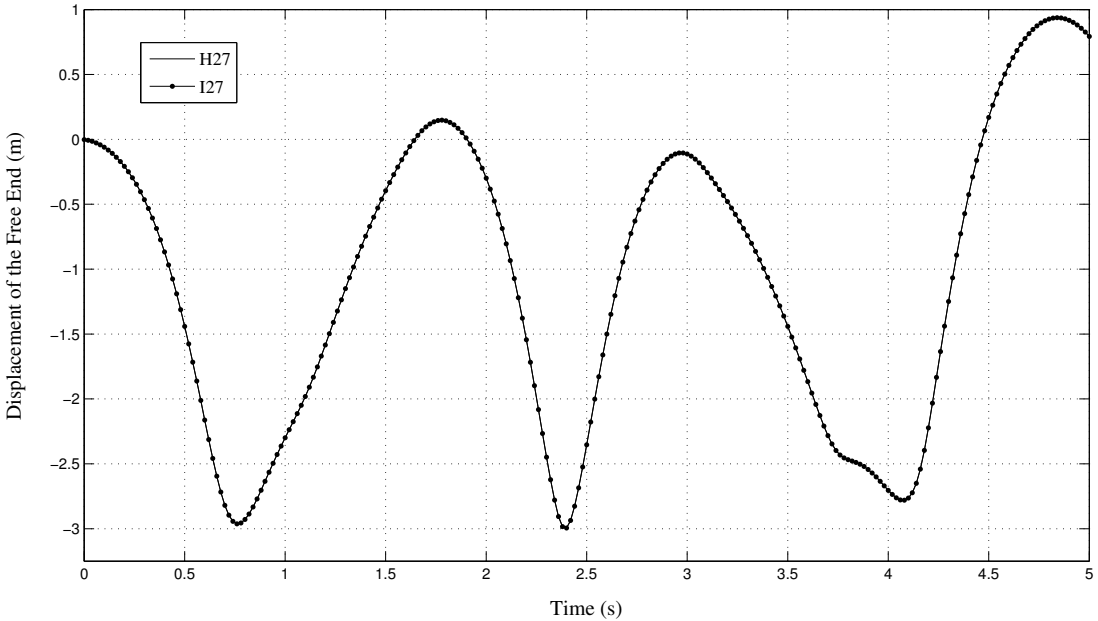


Figure 7. Time evolution of the vertical coordinate of the free end of the double pendulum.

modulus E , the Poisson's ratio, and the density are taken to be 9.81 m/s^2 , $7 \times 10^{10} \text{ N/m}^2$, 0.0 , and 2000 kg/m^3 , respectively. The double pendulum starts from rest in the horizontal position and falls under the action of gravity. The motion is studied in the interval $[0, 5]$ seconds with $t_{\Delta} = 0.02 \text{ s}$ (which is twenty times that used in [Cuadrado et al. 2001]). Two H27/I27 elements (one element per link) are used to carry out the simulation. The time evolution of the vertical coordinate of the free end of the double pendulum is shown in Figure 7, which is found to agree very well with the corresponding result presented in [Cuadrado et al. 2001, Figure 7]. The snapshots of the motion at one second intervals are shown in Figure 8. As in the single link pendulum of the previous example, the total energy (kinetic, strain, and potential) is conserved. Although the results obtained using the I27 element are almost identical to those obtained using the H27 element, the total number of iterations is much larger (4 to 5 iterations per time step for the H27 element versus 6 to 7 iterations per time step for the I27 element).

4.3. Dynamics of a tumbling cylinder. The dynamics of a short elastic cylinder, initially at rest, and subjected to an impulsive load have been studied by several researchers [Simo and Tarnow 1994; Brank et al. 1998; Balah and Al-Ghamedy 2005]. The geometry, finite element mesh for the H27 element, material parameters, and loading conditions are shown in Figure 9. The loads mentioned in Figure 9 are distributed across the height in a consistent manner. The simulation is carried out over the time interval $[0, 25]$ seconds with a time step $t_{\Delta} = 0.02 \text{ s}$. The cylinder is discretized using a mesh of 2×16 H27/I27 elements, and an equivalent mesh for H8 elements. The sequence of deformed shapes at 2 second intervals is depicted in Figure 10. Figures 11, 12, and 13 show the time history of the linear and angular momentum vector components, and the total (kinetic and strain) energy; the results of the H27 element are in very good agreement with the results presented in [Brank et al. 1998; Balah and Al-Ghamedy 2005]. In accordance with the design of the algorithm, these quantities are conserved after

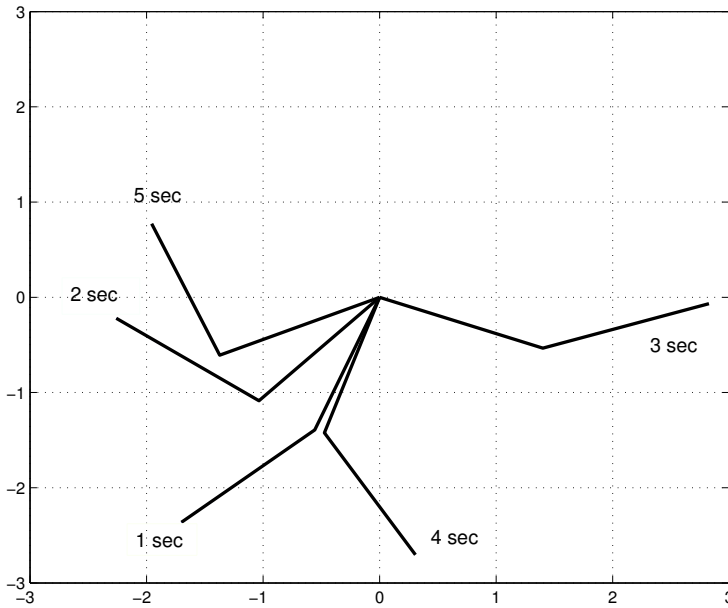


Figure 8. Snapshots of the motion of the double pendulum at one second intervals.

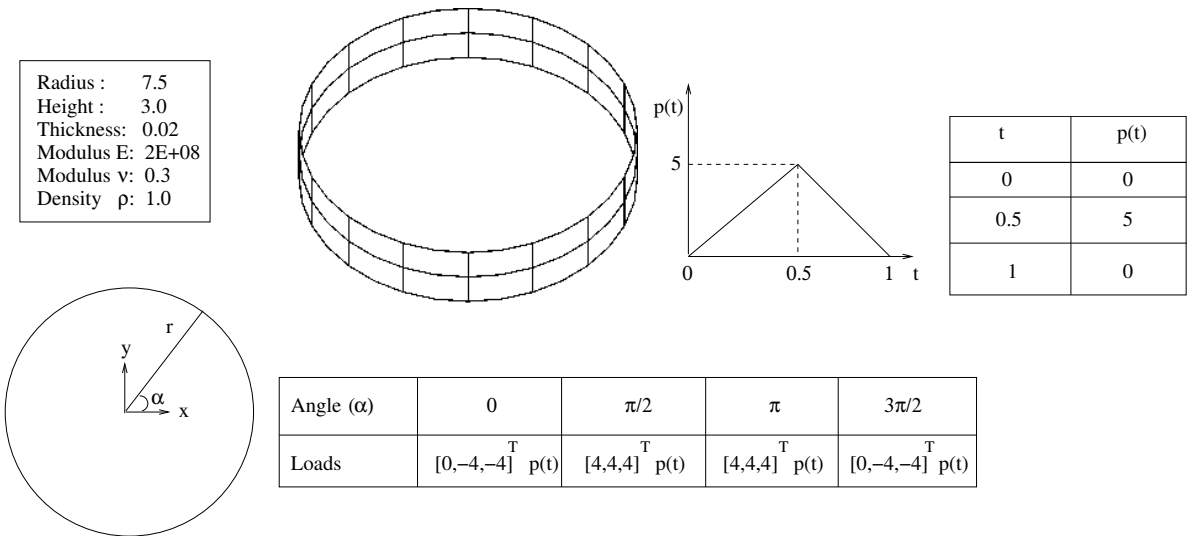


Figure 9. Short cylinder subjected to an impulsive load: geometry, material parameters, and loading conditions.

the removal of the external loads. Although the same linear momentum values are obtained using the H8 and I27/H27 elements, the angular momentum and energy values predicted by the H8 and I27 elements are different than those predicted by the H27 element, which indicates that they are susceptible to locking. One additional level of spatial refinement of the H8 element mesh yielded the same values of momentum and energy as the H27 element mesh. The algorithm also gave almost the same solution for $t_{\Delta} = 0.03$ s.



Figure 10. Sequence of deformed shapes of the tumbling cylinder at 2 second intervals.

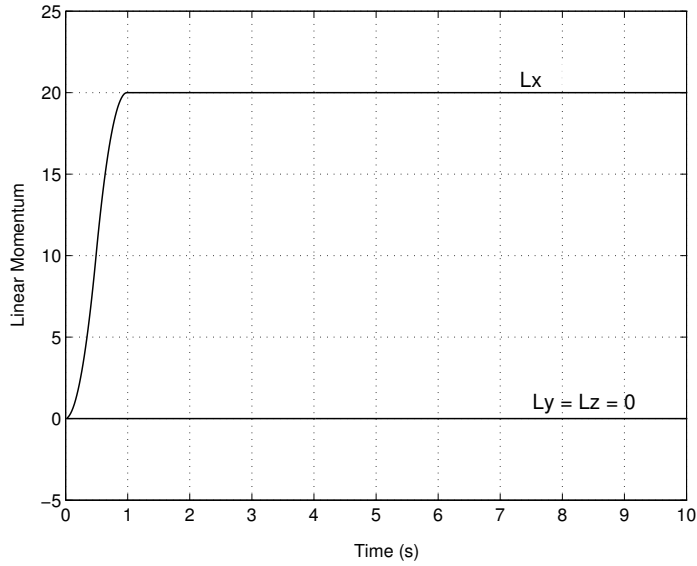


Figure 11. Tumbling cylinder: time history of linear momentum.

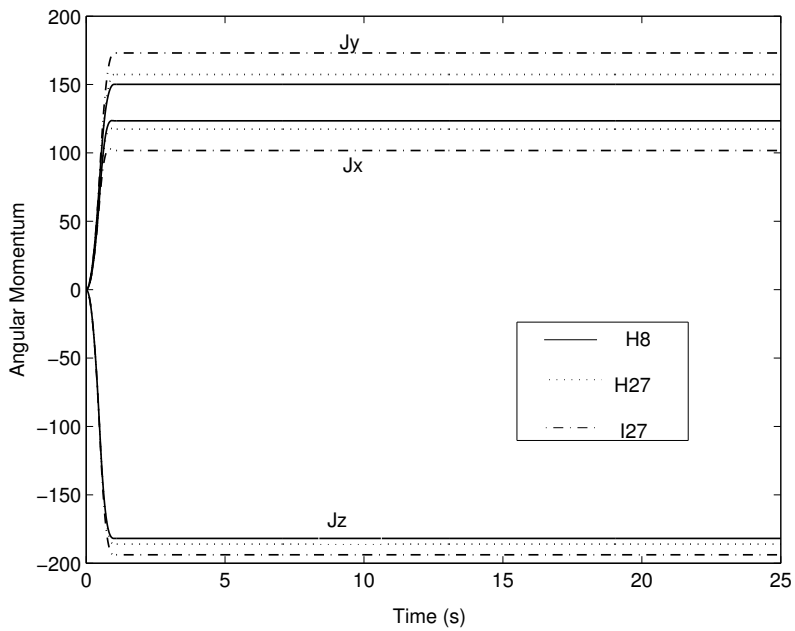


Figure 12. Tumbling cylinder: time history of angular momentum.

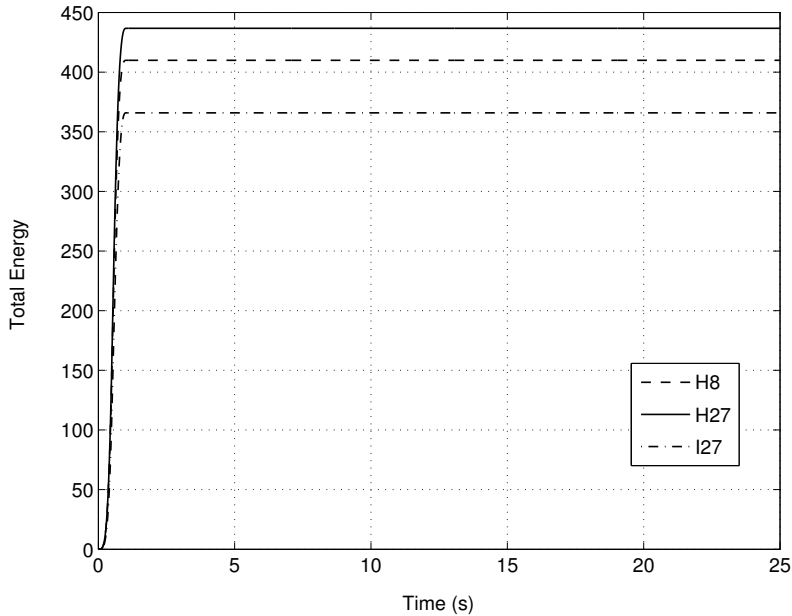


Figure 13. Tumbling cylinder: time history of total energy.

4.4. Snap-through of a cylindrical shell under concentrated vertex load. This dynamic-buckling problem has been studied by several researchers [Kuhl and Ramm 1996; 1999; Balah and Al-Ghamedy 2005]. The geometry, boundary conditions, material properties, and loading are shown in Figure 14. Two edges are simply supported as shown, and the load $R(t)$ is applied at the center of the panel. The panel first undergoes snap-through, and then shows high-frequency dominated behavior in the postbuckling phase. Due to symmetry, only one fourth of the domain is discretized using $4 \times 4 \times 1$ H27/I27 elements, and $8 \times 8 \times 2$ H8 elements, and we use a time step of $t_{\Delta} = 0.001$ s as in [Balah and Al-Ghamedy 2005]. The solutions obtained using the H27/I27 and H8 elements are shown in Figure 15; the H8 element results are in very good agreement with the third-order shear deformation theory-based element results presented in [Balah and Al-Ghamedy 2005, Figure 8]. Once again we see that the I27 and H8 elements are susceptible to locking. Refining the H8 element mesh to $16 \times 16 \times 2$ yields the same solution as the H27 element solution. We note that unlike Kuhl and Ramm [1999], we obtain the solution for $t_{\Delta} = 0.001$ s without adding any numerical dissipation or using reduced integration, and the number of iterations was also much less (around 6 iterations per time step). The snapshots of the snap-through process are shown in Figure 16.

4.5. Bar impact problem. This example has been considered in [Bauchau and Joo 1999]. A bar of length 4 m, square cross-section of dimension 1, Young's modulus $E = 1 \text{ N/m}^2$, Poisson's ratio $\nu = 0$, and density $\rho_0 = 1 \text{ kg/m}^3$, travelling at a constant longitudinal velocity $v_0 = 10^{-3} \text{ m/s}$ impacts a rigid wall at time $t = 0$. This impact results in a compressive stress wave which propagates with constant velocity from the left end of the bar to the right end. At time $t = 0$, all the nodes except those on the impacting face are given an initial velocity 10^{-3} m/s , and at subsequent times, the nodes on the impacting face

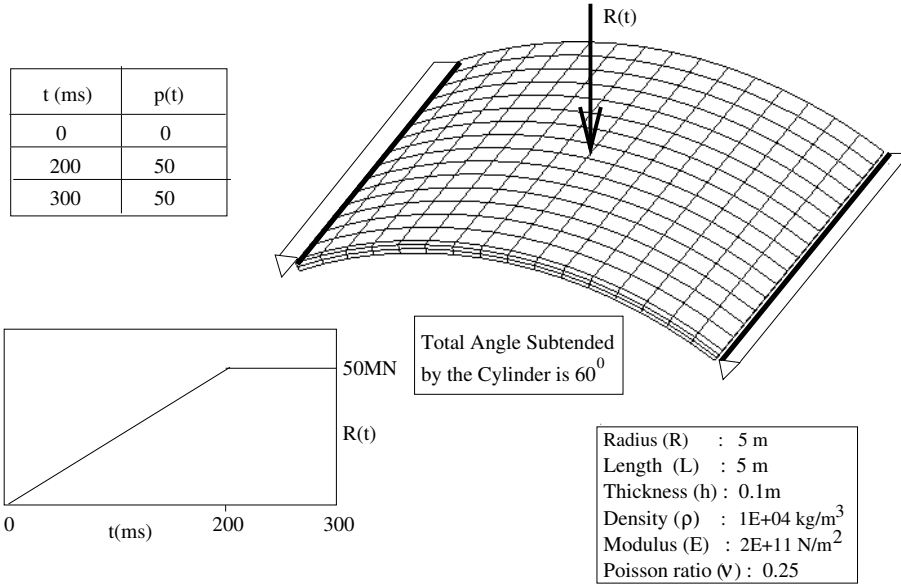


Figure 14. Dynamic buckling of a panel: geometry, material parameters and loading conditions.

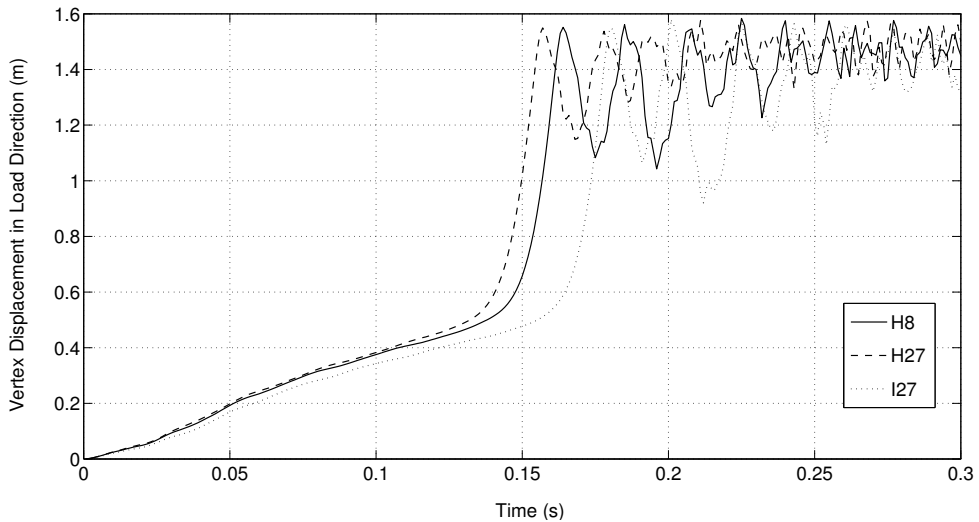


Figure 15. Snap-through of a panel: time history of the vertical displacement under the load for $t_\Delta = 0.001$.

are constrained. A time step of $t_\Delta = 0.01$ s is used. Meshes of 400 and 800 H27/I27 elements (along the length) and 1600 H8 elements are used to discretize the structure. Figure 17 shows the axial stress distribution for $x \in [2, 3]$ meters (for greater clarity) at $t = 2.56$ s, at which time the compressive stress wave is located at $x = 2.56$ m. Identical results as with the H27 element are obtained with the I27 element. In contrast with the results shown in [Bauchau and Joo 1999, Figure 14], where increasing the spatial refinement resulted in an increase in the error, with our formulation, the errors remain the same

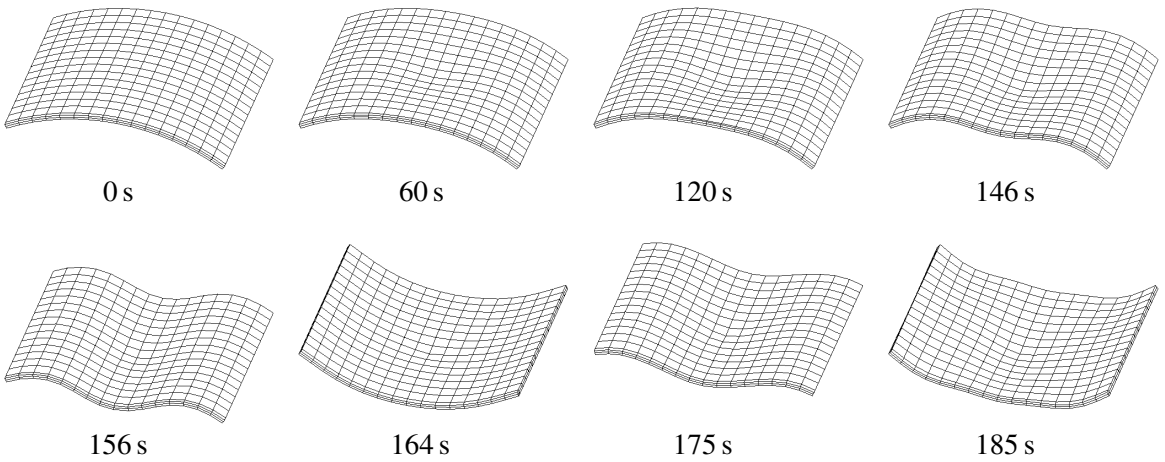


Figure 16. Panel problem: snapshots of the snap-through process.

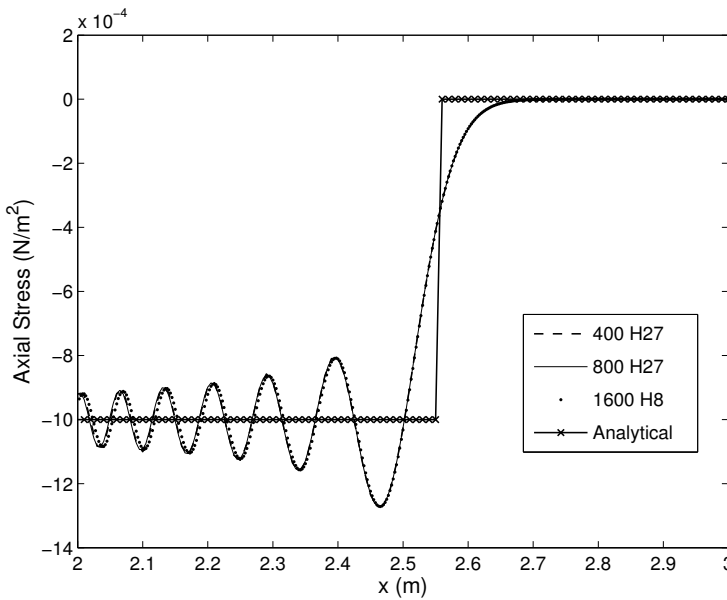


Figure 17. Bar impact problem: axial stress at time $t = 2.56$ s obtained with the energy-conserving scheme.

with spatial mesh refinement (keeping t_{Δ} fixed), thus bypassing the need for high-frequency dissipation (although, of course, introducing dissipation does smooth out the solution as discussed below). Reducing the t_{Δ} resulted in reduced amplitude and increased frequency in the oscillations. Figure 18 shows the temporal variation of the axial stress at $x = 1$ m obtained using the energy-conserving scheme.

The results obtained with the energy-dissipative scheme with α set to 0.001 are shown in Figure 19. The oscillations are damped out, and the solution is quite close to the exact solution. The decay in energy as a function of time is shown in Figure 20.

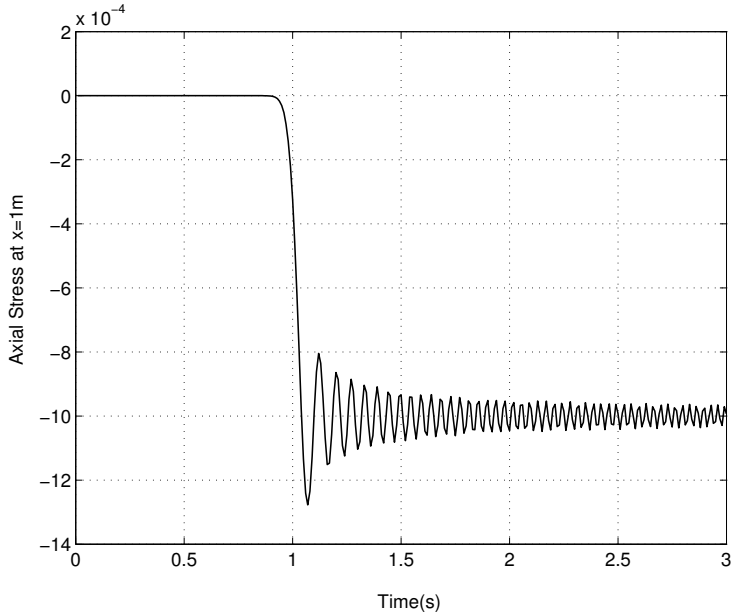


Figure 18. Bar impact problem: temporal variation of the axial stress at $x = 1$ m obtained with the 800 element H27 mesh and the energy-conserving scheme.

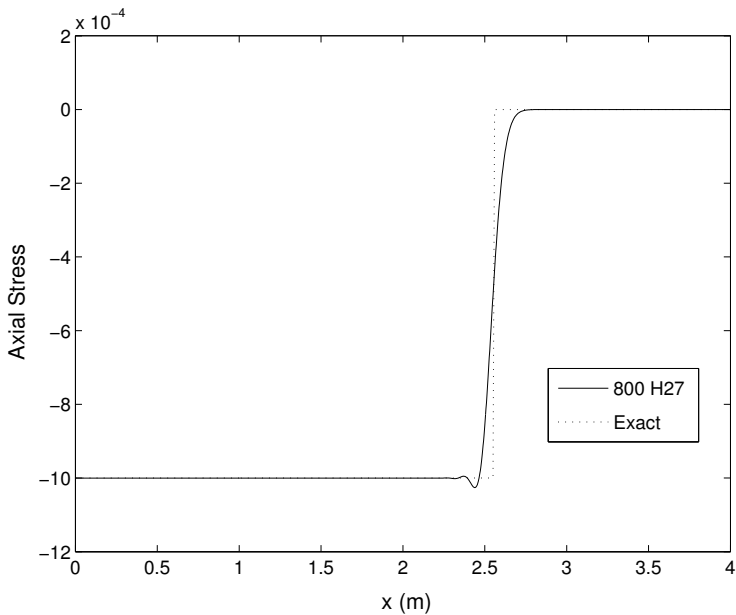


Figure 19. Bar impact problem: axial stress at time $t = 2.56$ s obtained with the energy-dissipative scheme.

The instabilities that arise in the solution with an inappropriate choice of the stress interpolation (see [Section 3.3](#)) occur around $t = 1.6$ s in the region near the impacting surface.

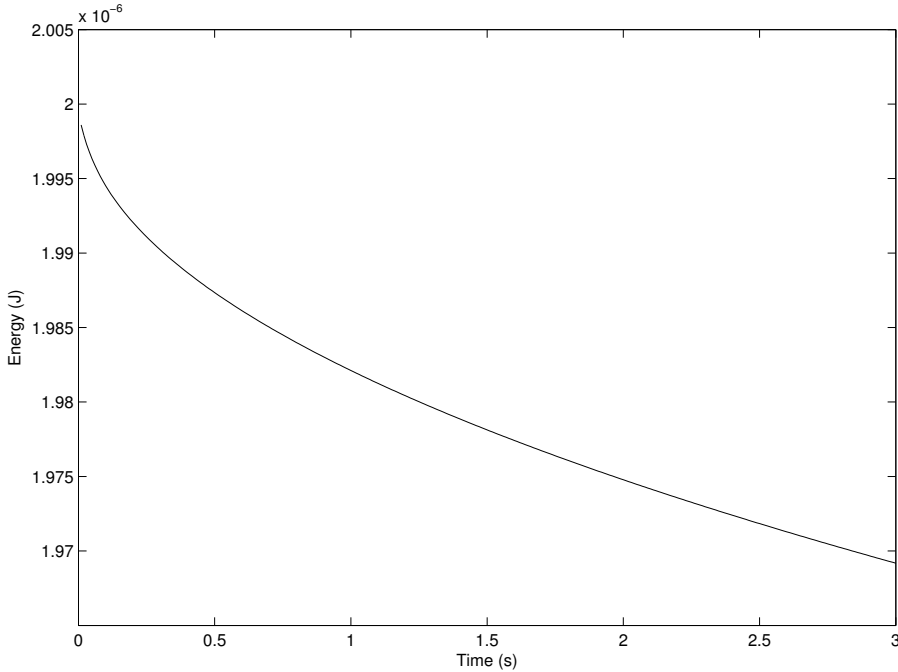


Figure 20. Bar impact problem: temporal variation of the energy obtained with the energy-dissipative scheme.

4.6. Motion of toss rule in space. This example shows the performance of the proposed algorithm when the motion is three-dimensional, and the forces are such that they cause bending, shear, and torsional deformations, and translational and rotational motion of the body [Kuhl and Ramm 1996; 1999]. The geometry, loads, and material properties are shown in Figure 21. The same time step as in [Kuhl and Ramm 1996; 1999], $t_{\Delta} = 50 \times 10^{-6}$, is used, and a mesh of 6×1 H27 elements is used. Simulations are also carried out using a refined mesh of 15×2 H27/I27 elements. The snapshots of the results until

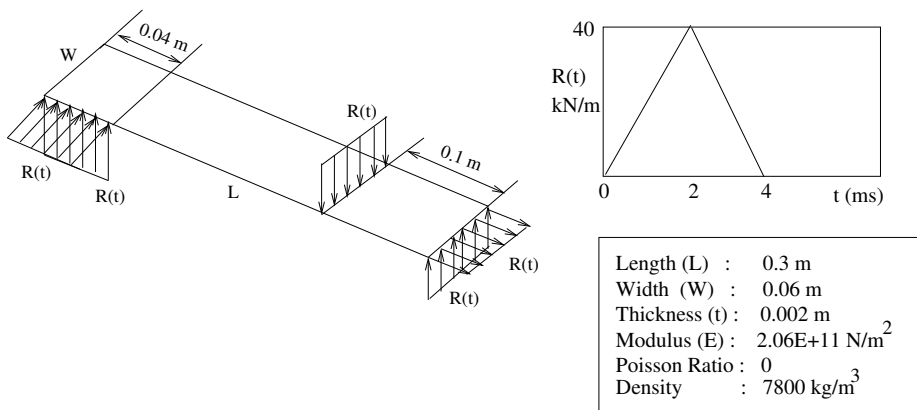


Figure 21. Toss rule problem: geometry, loads and material properties.

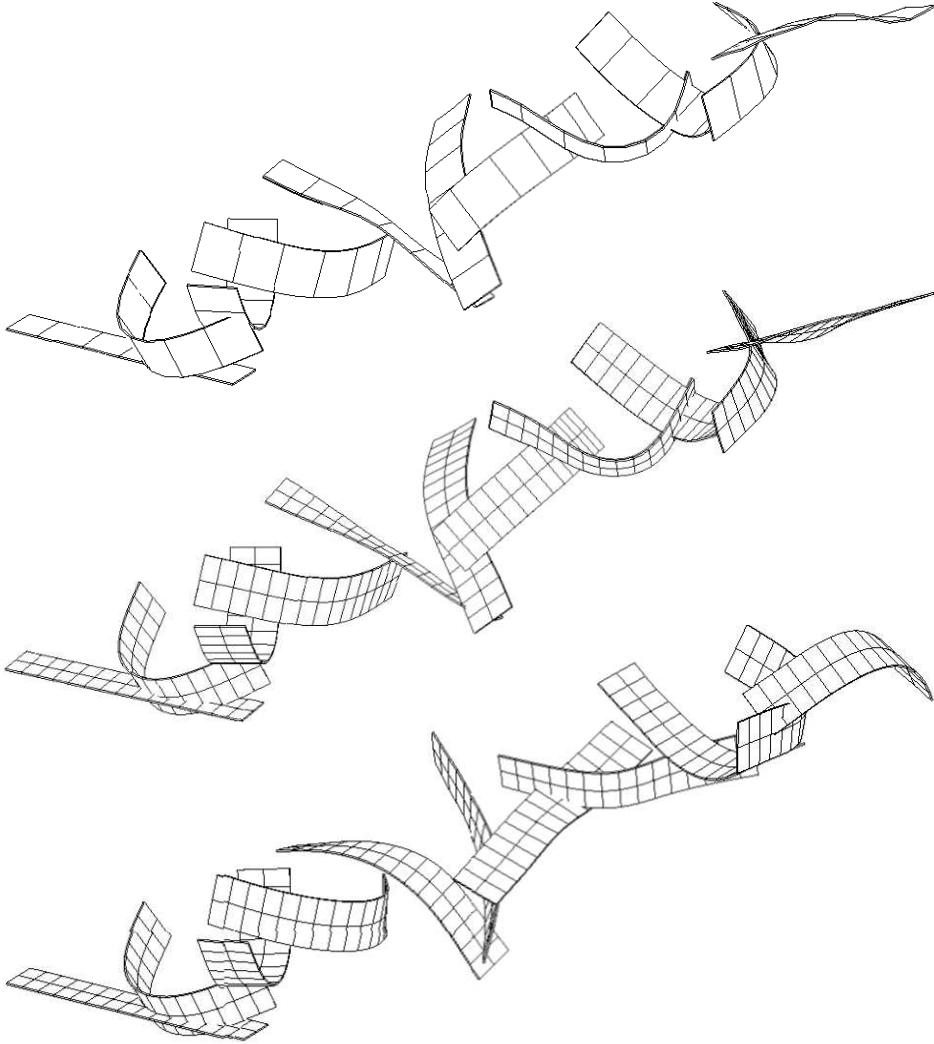


Figure 22. Motion of the toss rule obtained using a 6×1 H27 mesh (top), a 15×2 H27 mesh (middle) and a 15×2 I27 mesh (bottom).

$t = 0.04$ s at intervals of 0.004 s are shown in [Figure 22](#), and there is almost perfect agreement with the results presented in [\[Kuhl and Ramm 1999\]](#) until $t = 0.032$ s, and slight deviations thereafter. A possible explanation for the deviations might be that Kuhl and Ramm use numerical dissipation to compensate for the energy increase that they encounter due to the use of reduced integration (to prevent shear locking of their shell element). In contrast, no shear locking is observed even with the coarse H27 mesh, and the linear momentum, angular momentum, and energy are perfectly conserved after the removal of the loads, as seen in [Figure 23](#). Note that although the energy plot obtained using the I27 element is almost identical to that obtained using the H27 element, the motions are very different (compare the last two parts of [Figure 22](#)). This is because the total energy is obtained by integrating over the entire domain, so that different displacement and velocity fields can yield almost identical total energy values.

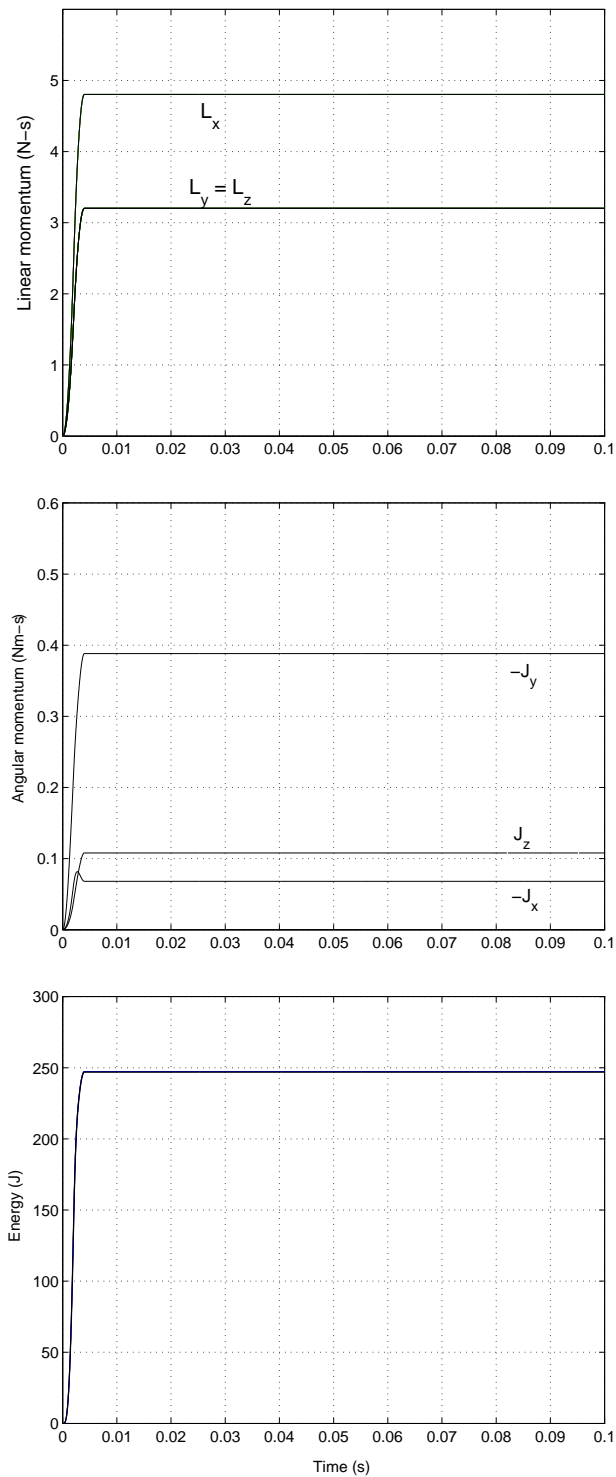


Figure 23. Toss rule problem: time history of the linear momentum (top), angular momentum (middle) and energy (bottom: H8, H27 and I27 elements).

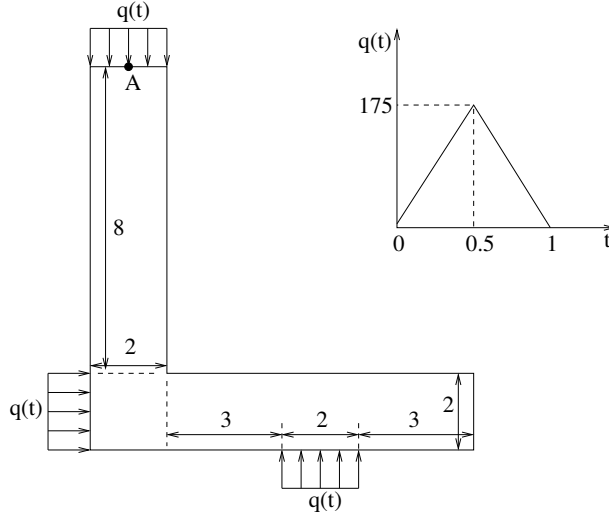


Figure 24. L-block problem: geometry and loading conditions.

4.7. L-block problem. This problem, paralleling one in [Betsch and Steinmann 2001], demonstrates the performance of the algorithm when the material model is nonlinear. An L-block under plane strain conditions is subjected to the loads shown in Figure 24. A compressible neoHookean material model with the strain-energy density function and the corresponding stress-strain relation given by

$$\hat{W} = \frac{\lambda}{8} (\ln \det \mathbf{C})^2 + \frac{\mu}{2} (\text{tr } \mathbf{C} - 3 - \ln \det \mathbf{C}), \quad \mathbf{S} = \frac{\lambda}{2} (\ln \det \mathbf{C}) \mathbf{C}^{-1} + \mu (\mathbf{I} - \mathbf{C}^{-1}).$$

is used with $\lambda = 2000$ and $\mu = 1000$. The density is $\rho_0 = 1$. A uniform mesh of 144 H27 elements is used to discretize the structure. Since the material is extremely flexible, a time step of $t_\Delta = 10^{-4}$ is used to capture the transients. The time histories of the x component of the linear momentum, the z component of the angular momentum, and the total (kinetic and strain) energy are shown in Figure 25. These values are seen to be constant after the removal of the loading. As seen in the bottom part of the figure, the energy value after the removal of the loads is 3340, while the corresponding value obtained using a coarser mesh of 36 uniform elements is 3328, showing that our mesh density is sufficient to capture the transient behavior. The (u_x, u_y) displacements of the midpoint of the top edge (point A in Figure 24) as a function of time are shown in Figure 26.

The example presented in [Betsch and Steinmann 2001] had the same geometry, but the parameters were $\lambda = 1000$, $\mu = 500$, and $\rho_0 = 0.5$. The solution given there is an unconverged solution, with a final energy value of roughly 3500, while we get a value of around 7700 with the 144-element mesh. However, a very fine time step is required to obtain this solution, and hence we have used the higher values of the material parameters given above.

5. Conclusions

A new energy-momentum conserving hybrid-stress formulation for conducting the transient analysis of nonlinear elastic structures has been presented. Since hybrid elements are less susceptible to locking compared to displacement-based elements, they can be used to conduct the transient analysis of

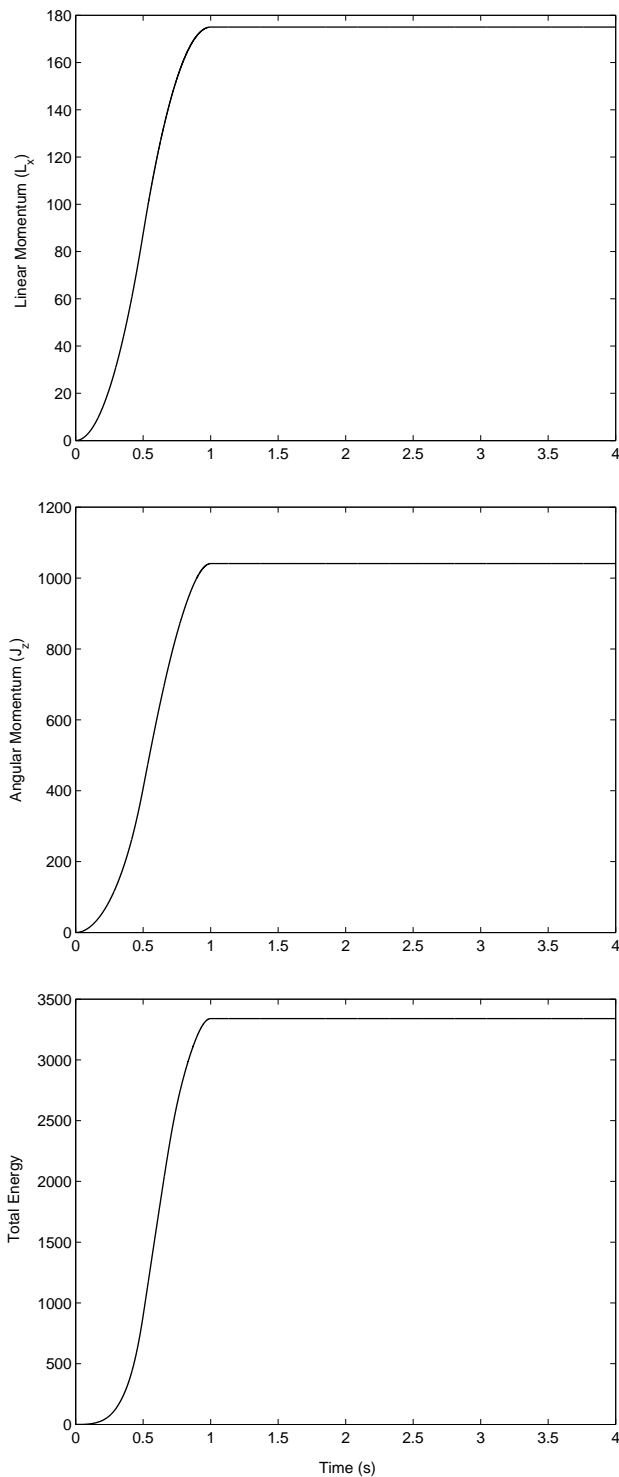


Figure 25. L-block problem: time history of the x component of the linear momentum (top), the z component of the angular momentum (middle), and total energy (bottom).

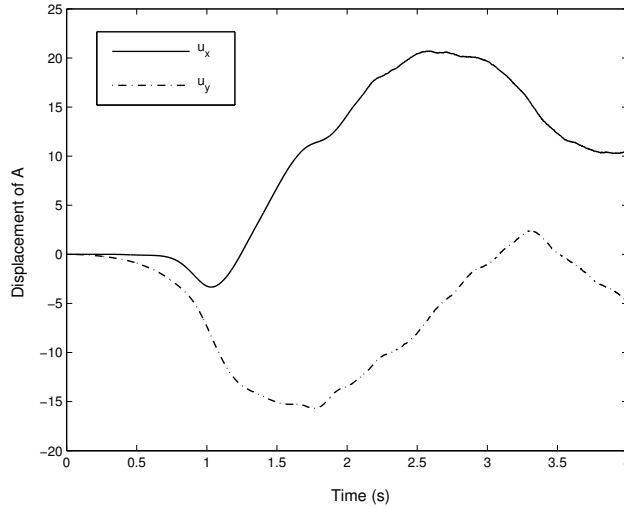


Figure 26. L-block problem: (u_x, u_y) displacements of point A.

beams/plates/shells, as well as “chunky” 3D structures, in an economical way. Good coarse-mesh accuracy is obtained even on demanding problems such as the panel buckling and toss rule problems, and since there appears to be no degradation in accuracy with mesh refinement (for a given time step), as opposed to some other strategies presented in the literature, an algorithmic modification that would dissipate higher frequencies introduced due to mesh refinement does not appear to be necessary. An exact tangent stiffness matrix has been formulated and used, resulting in a quadratic rate of convergence in the vicinity of the solution, and thereby resulting in a reduced number of iterations per time step compared with other strategies. Finally, since the stress parameters are condensed out at an element level, and the user works only with displacement degrees of freedom, the same input data structure used for standard displacement-based isoparametric hexahedral elements can also be used for these elements. Extensions of the current work to large-deformation plasticity and to contact problems would obviously be of interest.

References

- [Armero and Romero 2001a] F. Armero and I. Romero, “On the formulation of high-frequency dissipative time-stepping algorithms for nonlinear dynamics, I: Low-order methods for two model problems and nonlinear elastodynamics”, *Comput. Methods Appl. Mech. Eng.* **190**:20-21 (2001), 2603–2649.
- [Armero and Romero 2001b] F. Armero and I. Romero, “On the formulation of high-frequency dissipative time-stepping algorithms for nonlinear dynamics, II: Second-order methods”, *Comput. Methods Appl. Mech. Eng.* **190**:51-52 (2001), 6783–6824.
- [Balah and Al-Ghamedy 2005] M. Balah and H. N. Al-Ghamedy, “Energy-momentum conserving algorithm for nonlinear dynamics of laminated shells based on a third-order shear deformation theory”, *J. Eng. Mech. (ASCE)* **131**:1 (2005), 12–22.
- [Bauchau and Joo 1999] O. A. Bauchau and T. Joo, “Computational schemes for non-linear elasto-dynamics”, *Int. J. Numer. Methods Eng.* **45**:6 (1999), 693–719.
- [Bauchau et al. 2003] O. A. Bauchau, C. L. Bottasso, and L. Trainelli, “Robust integration schemes for flexible multibody systems”, *Comput. Methods Appl. Mech. Eng.* **192**:3-4 (2003), 395–420.

- [Betsch and Steinmann 2001] P. Betsch and P. Steinmann, “Conservation properties of a time FE method, II: Time-stepping schemes for non-linear elastodynamics”, *Int. J. Numer. Methods Eng.* **50**:8 (2001), 1931–1955.
- [Brank et al. 1998] B. Brank, L. Briseghella, N. Tonello, and F. B. Damjanić, “On non-linear dynamics of shells: implementation of energy-momentum conserving algorithm for a finite rotation shell model”, *Int. J. Numer. Methods Eng.* **42**:3 (1998), 409–442.
- [Cuadrado et al. 2001] J. Cuadrado, R. Gutiérrez, M. A. Naya, and M. P., “A comparison in terms of accuracy and efficiency between a MBS dynamic formulation with stress analysis and a non-linear FEA code”, *Int. J. Numer. Methods Eng.* **51**:9 (2001), 1033–1052.
- [Gonzalez 2000] O. Gonzalez, “Exact energy and momentum conserving algorithms for general models in nonlinear elasticity”, *Comput. Methods Appl. Mech. Eng.* **190**:13-14 (2000), 1763–1783.
- [Gupta 2000] A. Gupta, “WSMP: Watson Sparse Matrix Package, Part II – direct solution of general sparse systems”, Research Report RC 21888 (98472), IBM Corporation, Yorktown Heights, NY, 2000, Available at <http://www-users.cs.umn.edu/~agupta/doc/wsm2.pdf>.
- [Gupta 2002] A. Gupta, “Recent advances in direct methods for solving unsymmetric sparse systems of linear equations”, *ACM Trans. Math. Software* **28**:3 (2002), 321–324.
- [Jog 2005] C. S. Jog, “A 27-node hybrid brick and a 21-node hybrid wedge element for structural analysis”, *Finite Elem. Anal. Des.* **41**:11–12 (2005), 1209–1232.
- [Jog and Annabattula 2006] C. S. Jog and R. Annabattula, “The development of hybrid axisymmetric elements based on the Hellinger–Reissner variational principle”, *Int. J. Numer. Methods Eng.* **65**:13 (2006), 2279–2291.
- [Jog and Kelkar 2006] C. S. Jog and P. P. Kelkar, “Non-linear analysis of structures using high performance hybrid elements”, *Int. J. Numer. Methods Eng.* **68**:4 (2006), 473–501.
- [Kuhl and Crisfield 1999] D. Kuhl and M. A. Crisfield, “Energy-conserving and decaying algorithms in non-linear structural dynamics”, *Int. J. Numer. Methods Eng.* **45**:5 (1999), 569–599.
- [Kuhl and Ramm 1996] D. Kuhl and E. Ramm, “Constraint energy momentum algorithm and its application to non-linear dynamics of shells”, *Comput. Methods Appl. Mech. Eng.* **136**:3-4 (1996), 293–315.
- [Kuhl and Ramm 1999] D. Kuhl and E. Ramm, “Generalized energy-momentum method for non-linear adaptive shell dynamics”, *Comput. Methods Appl. Mech. Eng.* **178**:3-4 (1999), 343–366.
- [Laursen and Meng 2001] T. A. Laursen and X. N. Meng, “A new solution procedure for application of energy-conserving algorithms to general constitutive models in nonlinear elastodynamics”, *Comput. Methods Appl. Mech. Eng.* **190**:46-47 (2001), 6309–6322.
- [Lee and Rhiu 1986] S. W. Lee and J. J. Rhiu, “A new efficient approach to the formulation of mixed finite element models for structural analysis”, *Int. J. Numer. Methods Eng.* **23**:9 (1986), 1629–1641.
- [Pian and Sumihara 1984] T. H. H. Pian and K. Sumihara, “Rational approach for assumed stress finite elements”, *Int. J. Numer. Methods Eng.* **20**:9 (1984), 1685–1695.
- [Pian and Tong 1986] T. H. H. Pian and P. Tong, “Relations between incompatible displacement model and hybrid stress model”, *Int. J. Numer. Methods Eng.* **22**:1 (1986), 173–181.
- [Sansour et al. 2004] C. Sansour, P. Wriggers, and J. Sansour, “On the design of energy-momentum integration schemes for arbitrary continuum formulations: applications to classical and chaotic motion of shells”, *Int. J. Numer. Methods Eng.* **60**:15 (2004), 2419–2440.
- [Simo and Tarnow 1992] J. C. Simo and N. Tarnow, “The discrete energy-momentum method: conserving algorithms for nonlinear elastodynamics”, *Z. Angew. Math. Phys.* **43**:5 (1992), 757–792.
- [Simo and Tarnow 1994] J. C. Simo and N. Tarnow, “A new energy and momentum conserving algorithm for the non-linear dynamics of shells”, *Int. J. Numer. Methods Eng.* **37**:15 (1994), 2527–2549.
- [Sze and Fan 1996] K. Y. Sze and H. Fan, “An economical assumed stress brick element and its implementation”, *Finite Elem. Anal. Des.* **21**:3 (1996), 179–200.
- [Xue et al. 1985] W.-M. Xue, L. A. Karlovitz, and S. N. Atluri, “On the existence and stability conditions for mixed-hybrid finite element solutions based on Reissner’s variational principle”, *Int. J. Solids Struct.* **21**:1 (1985), 97–116.

[Yakoub and Shabana 2001] R. Yakoub and A. A. Shabana, “Three dimensional absolute nodal coordinate formulation for beam elements: implementation and applications”, *J. Mech. Des. (ASME)* **123**:4 (2001), 614–621.

Received 23 Nov 2008. Revised 7 Jan 2009. Accepted 5 Feb 2009.

C. S. JOG: jogc@mecheng.iisc.ernet.in

Department of Mechanical Engineering, Indian Institute of Science, Bangalore 560012, India

PHANI MOTAMARRI: phani.255@gmail.com

Department of Mechanical Engineering, Indian Institute of Science, Bangalore 560012, India